

CANOE: Classically Assisted Non-Orthogonal Eigensolver

Jihyeon Park,^{1,*} Collin C. D. Frink,¹ and Matthew Otten^{1,2,†}

¹*Department of Physics, University of Wisconsin – Madison, Madison, WI 53706, USA*

²*Department of Chemistry, University of Wisconsin – Madison, Madison, WI 53706, USA*

In the early fault-tolerant regime, where quantum resources remain limited, hybrid quantum-classical strategies offer one possible route toward quantum advantage. We introduce CANOE, the Classically Assisted Non-Orthogonal Eigensolver, as such an approach, distributing Rayleigh–Ritz basis states between quantum and classical hardware. This approach leverages the expressive power of quantum states, which are costly to reproduce classically, while augmenting them with a large pool of classically generated basis states that can be incorporated at negligible computational cost. We validate this through numerical simulations of a 76-qubit chromium atom system, quantifying how each additional quantum basis state enhances ground-state representability and how the inclusion of classical states further amplifies this improvement. Such a hybrid basis framework necessarily requires an efficient protocol on quantum hardware for evaluating overlaps between quantum and classical states in the resulting generalized eigenvalue formulation. We address this by introducing a histogram-based protocol and demonstrate through numerical simulations that it can approach chemical accuracy at moderate sampling cost. To solve the resulting generalized eigenvalue problem stably, CANOE incorporates a Schur-complement-based stabilization procedure that mitigates ill-conditioning caused by linear dependencies in the hybrid basis. Taken together, these results position CANOE as a practical framework for combining limited quantum resources with expansive classical resources for early fault-tolerant quantum simulations.

I. INTRODUCTION

Quantum computers have the potential to provide distinct computational advantage for problems in chemistry and materials science [1, 2], especially with large-scale, fault-tolerant devices [3]. The pursuit of quantum advantage in quantum simulation remains an active effort in the early fault-tolerant regime [4–6]. Despite steady progress in hardware development, quantum devices continue to operate under constraints in coherence, gate fidelity, and feasible circuit depth [7]. Consequently, hybrid quantum–classical frameworks have emerged as a practical strategy for distributing computational workload between quantum and classical processors, thereby optimizing the use of scarce quantum resources [6, 8, 9]. The most representative example of such hybrid approaches is the variational quantum eigensolver (VQE), in which a quantum device prepares a parameterized ansatz state and measures expectation values, while a classical optimizer updates the circuit parameters [5, 6, 10–14]. Related hybrid quantum–classical optimization ideas have also been explored beyond electronic-structure settings, for example in combinatorial optimization problems [15].

More recently, a family of methods based on Rayleigh–Ritz subspace diagonalization has attracted increasing attention. The non-orthogonal variational quantum eigensolver (NOVQE) extends VQE by preparing multiple independently parameterized quantum ansatz states, measuring their Hamiltonian and overlap matrix elements, and classically solving a generalized eigenvalue problem [11]. The optimization-free nonorthogonal

quantum eigensolver (NOQE) removes the variational parameter-optimization loop by preparing quantum states with fixed parameters and directly solving the generalized eigenvalue problem [16]. Other related subspace methods—including quantum subspace expansion (QSE), quantum Krylov approaches, quantum filter diagonalization, and symmetry-structured variants such as Q-SENSE—differ primarily in how the quantum subspace is constructed, yet share a common hybrid workflow: quantum circuits prepare the basis states and estimate matrix elements, while classical routines perform the subsequent eigenvalue computation [8, 17–22]. In contrast, sample-based quantum diagonalization (SQD) adopts a different strategy: a quantum device generates a determinant subspace via sampling, while classical high-performance computing resources perform configuration recovery, subspace construction, and large-scale eigenvalue solving [23–25].

Against this landscape, we introduce CANOE (Classically Assisted Non-Orthogonal Eigensolver), a distinct level of classical–quantum hybridization. Rather than generating the subspace entirely on quantum hardware or constructing it purely from sampled determinants, CANOE hybridizes at the level of basis construction itself: quantum-prepared states form the expressive core of the subspace, while a large set of classically constructed states provides the addition of variational freedom. As a consequence, a significant portion of the projected matrix elements can be evaluated efficiently on classical hardware, reducing the quantum sampling burden while retaining quantum-generated expressivity.

This architecture, the combination of many inexpensive classically constructed basis states with a smaller set of quantum-prepared states, necessitates calculating the overlap matrix elements between classical basis states and quantum-prepared states. A naive approach would recon-

* park687@wisc.edu

† mjotten@wisc.edu

construct the quantum state via full state tomography and compute overlaps classically. However, full quantum state tomography requires resources that scale exponentially with the number of qubits, $O(4^n)$, rendering it infeasible beyond small systems [26]. This exponential scaling has motivated the development of more measurement-efficient techniques, such as classical shadow tomography, which enable estimation of many properties of a quantum state without reconstructing the full density matrix [27–30]. To address this challenge, we develop a histogram-based sampling strategy that directly estimates the required matrix elements between classical determinants and quantum-prepared states, significantly reducing sampling overhead compared to tomography-based and shadow approaches.

In addition to measurement considerations, constructing a hybrid classical–quantum subspace introduces a numerical challenge. Quantum-prepared states often exhibit substantial mutual overlap, and when combined with a large number of classical basis states, this can induce significant linear dependence within the total subspace. Such redundancy leads to ill-conditioning of the overlap matrix in the generalized eigenvalue problem, potentially amplifying sampling noise and causing numerical instability. To mitigate this issue, we adopt a Schur-complement-based formulation that avoids direct inversion of the ill-conditioned overlap matrix, thereby stabilizing the eigenvalue computation while preserving the physical content of the hybrid subspace [31–33].

In this work, we introduce the CANOE hybrid subspace framework and demonstrate its effectiveness for ground-state energy estimation across a range of molecular systems. The protocol is summarized in Figure 1. In Section II, we first analyze classical-quantum subspace hybridization and its representational capabilities through large-scale simulations of a strongly correlated 76-spin-orbital chromium benchmark system in an idealized infinite-shot limit. We then study sampling-based overlap estimation, focusing on a histogram-based method and on how sampling noise propagates to the ground-state energy error, and finally examine stabilization of the resulting generalized eigensolver for the non-orthogonal hybrid basis. In Section III, we discuss the main bottlenecks of CANOE and outline directions for further improvement. Detailed technical implementations of the hybrid ansatz construction, overlap-sampling protocol, and subspace-truncation strategy are presented in Section IV.

II. RESULTS

The objective of CANOE is to compute the ground-state energy of a second-quantized fermionic Hamiltonian to chemical accuracy. The electronic Hamiltonian is given by

$$\hat{H} = h_q^p \hat{a}_p^\dagger \hat{a}_q + \frac{1}{4} h_{qs}^{pr} \hat{a}_p^\dagger \hat{a}_r^\dagger \hat{a}_s \hat{a}_q, \quad (1)$$

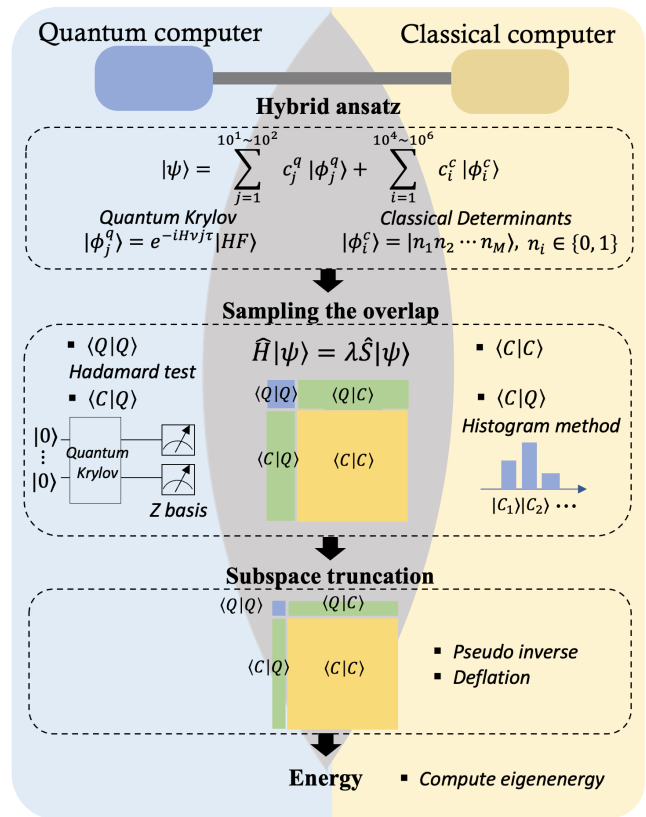


Figure 1. Overview of the CANOE protocol. The workload is distributed between classical (left) and quantum (right) processors. **Hybrid ansatz:** CANOE combines a large number of classical determinants with a small number of quantum-prepared states. **Sampling the overlap:** The projected matrices decompose into $\langle Q|Q \rangle$ (evaluated on quantum hardware using Hadamard test), $\langle C|C \rangle$ (computed on classical hardware), and $\langle Q|C \rangle$ blocks; the cross terms are estimated by sampling the quantum states and postprocessing classically via a histogram-based estimator. **Subspace truncation:** Ill-conditioning of the overlap matrix is mitigated entirely on classical hardware using a Schur-complement formulation with deflation or pseudo-inverse stabilization.

where h_q^p and h_{qs}^{pr} denote the one- and antisymmetrized two-electron integrals, respectively. Repeated indices imply summation, and \hat{a}_p^\dagger (\hat{a}_p) are fermionic creation (annihilation) operators acting on the corresponding spin orbitals. To solve the associated Schrödinger equation, CANOE constructs a hybrid classical–quantum subspace and performs a projected diagonalization within this basis.

A. Classical-Quantum Subspace Hybridization

The CANOE ansatz is defined as

$$|\psi\rangle = \sum_{i=1}^{N_c} c_i^c |\phi_i^c\rangle + \sum_{j=1}^{N_q} c_j^q |\phi_j^q\rangle, \quad (2)$$

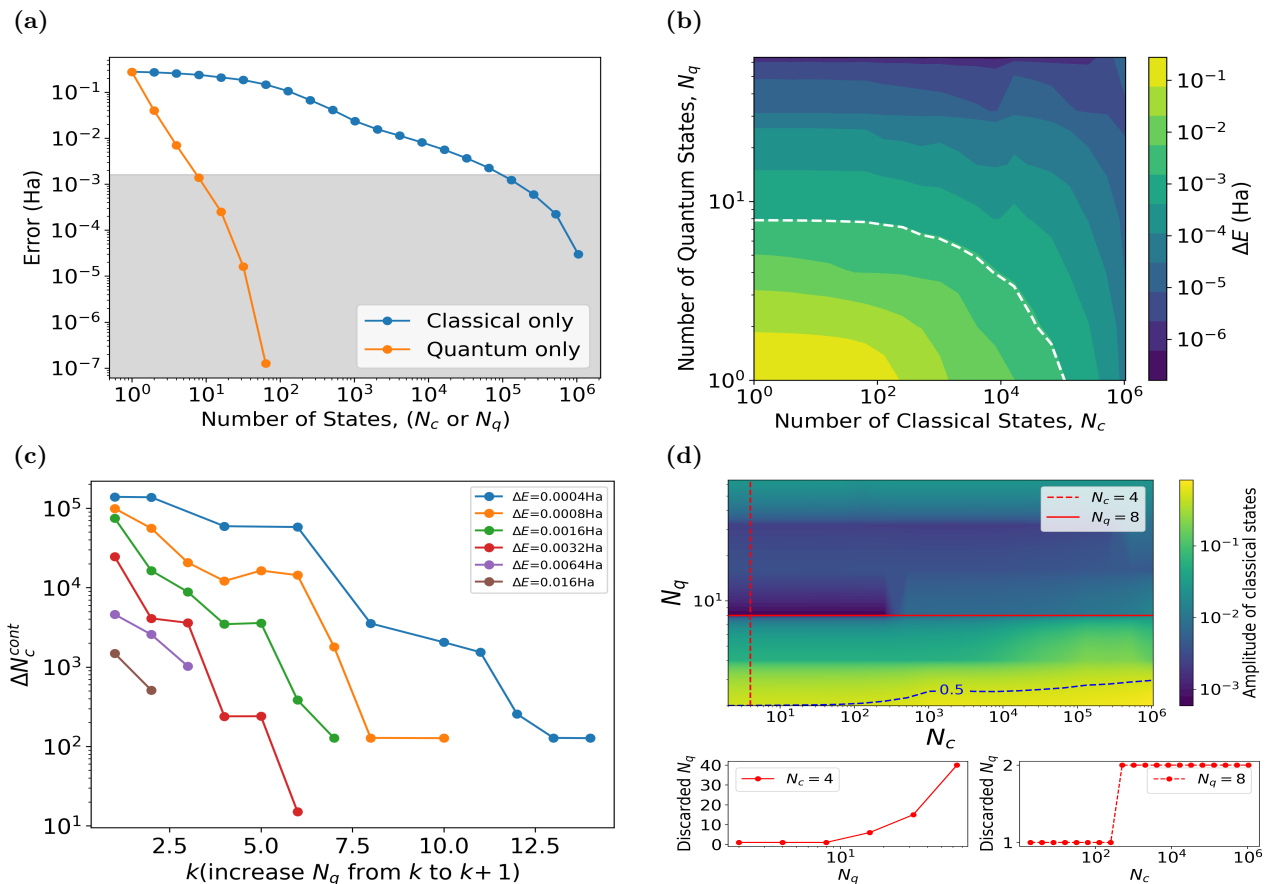


Figure 2. Classical-Quantum Subspace hybridization analysis on Cr system with 38 spatial orbitals and 14 electrons in cc-pVDZ-DK basis. **(a)**: ground-state energy error (Ha) versus basis-set size for a purely classical SHCI determinant (blue) and a purely quantum Krylov subspace (orange). The gray band indicates “chemical accuracy” (1.5936×10^{-3} Ha). **(b)**: ground-state energy error as a function of classical (N_c) and quantum (N_q) basis sizes. The white dashed line indicates the iso-error contour corresponding to chemical accuracy. **(c)**: marginal reduction in the number of classical basis states, ΔN_c^{cont} , that can be eliminated when one additional quantum basis state is introduced ($k \rightarrow k + 1$) while remaining on the same ground-state energy-error contour. **(d)**: ground-state classical-amplitude landscape over classical (N_c) and quantum (N_q) basis sizes. The color map shows the total classical amplitude $\sum_{i=1}^{N_c} |c_i|^2$ in the normalized ground state obtained from the generalized eigensolver. The contour labeled 0.5 marks the boundary where the classical and quantum sectors contribute equal weight. The bottom left and bottom right insets show the number of discarded quantum states along the lines $N_c = 4$ and $N_q = 8$, respectively, in the upper panel.

where $|\phi_i^c\rangle$ and $|\phi_j^q\rangle$ denote classical and quantum basis states, respectively. *Classical states* correspond to families of states for which the required overlap and Hamiltonian matrix elements remain classically tractable. In this work we restrict attention to determinants, which, as we demonstrate, are especially efficient. More generally, the classical sector could in principle include other states, such as Clifford states [34] or matrix product states [35]. *Quantum states* are prepared and measured on a quantum processor. Quantum states can also be any states that are substantially more efficient to prepare on quantum hardware than to represent classically. For example, they may be generated by ansätze such as unitary coupled cluster singles doubles (UCCSD) or hardware-efficient circuits [6, 13, 36]. In practice, CANOE targets a large number (10^4 – 10^6) of classical basis states and a small

number (10 – 10^2) of quantum basis states, reflecting realistic resource constraints of both classical and quantum hardware. In the occupation-number representation over M spin orbitals, the corresponding classical basis states are

$$|\phi_i^c\rangle = |n_1 n_2 \dots n_M\rangle, \quad n_k \in \{0, 1\}, \quad i = 0, 1, \dots, N_c, \quad (3)$$

The quantum basis states are defined as

$$|\phi_j^q\rangle = e^{-iH t_j} |HF\rangle, \quad j = 0, 1, \dots, N_q, \quad (4)$$

where H is the Hamiltonian of the system, $t_j = j \tau$ defines discrete time steps of size τ , and $|HF\rangle$ is the Hartree–Fock state. These states form a non-orthogonal Krylov subspace generated by time evolution of the Hartree–Fock reference state, chosen because Hamiltonian-generated

Krylov directions encode the system dynamics and can capture correlations that are difficult to reproduce within the truncated classical determinant space [18, 19, 21, 37]. The case $j = 0$ corresponds to the Hartree–Fock state $|HF\rangle$, which is also contained within the classical determinant space.

Projecting the Schrödinger equation for \hat{H} onto the hybrid basis $\{|\phi_\mu\rangle\} = \{|\phi_i^c\rangle\} \cup \{|\phi_j^q\rangle\}$ yields the generalized eigen-problem

$$\mathcal{H}\mathbf{c} = \lambda\mathcal{S}\mathbf{c}, \quad (5)$$

where $\mathcal{H}_{\mu\nu} = \langle\phi_\mu|\hat{H}|\phi_\nu\rangle$ and $\mathcal{S}_{\mu\nu} = \langle\phi_\mu|\phi_\nu\rangle$. The full workflow is summarized in Figure 1.

To validate the CANOE protocol, we consider a strongly correlated chromium atom in the cc-pVDZ-DK basis with 38 spatial orbitals (76 spin orbitals) and 14 electrons, corresponding to a 76-qubit representation. For computational efficiency, we only simulate the system in a restricted basis generated by the selection of only the most important determinants via a selected heat-bath configuration interaction (SHCI) [38] procedure, resulting in a sparse wavefunction simulator [39].

Before analyzing hybridization, we first examine purely classical and purely quantum subspaces. Figure 2(a) shows the ground-state energy error as a function of basis size for each case. The quantum Krylov subspace converges significantly faster: slightly more than 8 quantum states are sufficient to reach chemical accuracy, whereas nearly 10^5 classical determinants are required to achieve comparable precision. This highlights the strong expressive power of the quantum-generated directions.

We next vary both N_c and N_q simultaneously. Figure 2(b) presents the infinite-shot ground-state error over the (N_c, N_q) plane. Consistent with Figure 2(a), the error gradient is much steeper along the N_q direction, indicating that adding quantum states yields a larger marginal improvement. Nevertheless, increasing either N_c or N_q improves the energy across the surface, demonstrating that classical and quantum basis states augment the subspace in complementary ways. The white dashed line marks the iso-error contour corresponding to chemical accuracy, thereby delineating the combinations of (N_c, N_q) that are sufficient to reach this threshold. Around the elbow of this contour, near $N_q \sim 5$ and $N_c \sim 10^4$, the plot provides a useful example of the local tradeoff between the two sectors: as quantified more directly in Figure 2(c), increasing the quantum basis from $N_q = 5$ to $N_q = 6$ allows the classical basis size required for chemical accuracy to be reduced by roughly 3×10^3 determinants, whereas decreasing from $N_q = 5$ to $N_q = 4$ requires a comparable increase in N_c to remain on the same contour. Thus, the elbow reflects a real change in the marginal replacement power of additional quantum states.

To quantify this complementarity, Figure 2(c) analyzes the reduction in the number of classical determinants that can be eliminated when one additional quantum state is introduced while remaining on the same iso-error contour. The first added quantum state replaces the largest number

of classical determinants, reflecting that it introduces a direction most orthogonal to the classical subspace. Subsequent quantum states exhibit diminishing replacement power, as the most significant missing correlations have already been captured. Notably, the replacement effect becomes more pronounced in the high-accuracy regime, where classical improvements alone become increasingly costly. At the same time, this increased replaceability can signal that newly added quantum directions are only weakly independent of an already enriched hybrid basis, leading to near-redundancy and motivating deflation of such directions in the generalized eigensolver, which we discuss in more depth in Section II C.

Finally, Figure 2(d) examines how the ground-state amplitude is distributed between classical and quantum sectors. The color map shows the total classical weight $\sum_{i=1}^{N_c} |c_i|^2$ in the normalized ground state. For very small N_q , the classical sector carries most of the weight. However, as additional quantum states are introduced, the quantum sector rapidly accounts for a dominant portion of the expressivity. The first quantum state is omitted from the graph because it is identical to the Hartree–Fock reference already included in the classical determinant space. The non-smooth features observed in the landscape reflect truncation of nearly linearly dependent quantum directions. Section II C provides a detailed description of how we handle linear dependencies in the generalized eigenvalue problem, which includes discarding linearly-dependent directions. Along fixed lines $N_c = 4$ and $N_q = 8$, we observe that the number of discarded quantum states increases as more are added, indicating growing redundancy. Therefore, increasing N_q beyond a certain point does not necessarily yield proportional gains and must be balanced against resource cost. This also points to the need for more efficient selection of quantum states, perhaps through choosing different time schedules.

B. Overlap Estimation

Since CANOE uses a hybrid classical-quantum subspace, the overlap matrix \mathcal{S} naturally decomposes into three blocks: \mathcal{S}^{cc} , \mathcal{S}^{cq} , and \mathcal{S}^{qq} :

$$\mathcal{S} = \begin{pmatrix} \mathcal{S}^{cc} & \mathcal{S}^{cq} \\ \mathcal{S}^{qc} & \mathcal{S}^{qq} \end{pmatrix}, \quad (6)$$

where

$$\mathcal{S}_{ik}^{cc} = \langle\phi_i^c|\phi_k^c\rangle, \quad \mathcal{S}_{il}^{cq} = \langle\phi_i^c|\phi_l^q\rangle, \quad (7)$$

$$\mathcal{S}_{jk}^{qc} = \langle\phi_j^q|\phi_k^c\rangle, \quad \mathcal{S}_{jl}^{qq} = \langle\phi_j^q|\phi_l^q\rangle. \quad (8)$$

The N_c^2 classical–classical block is simply the identity matrix, and the N_q^2 quantum–quantum block can be measured using the Hadamard test in the quantum node, as is proposed in the standard NOQE scheme [16]. Our main focus is therefore the $N_c \times N_q$ classical–quantum block, namely how to efficiently estimate the projection

of a quantum state onto a classical state, including both its magnitude and phase, without resorting to expensive quantum tomography or using a large number of Hadamard tests.

As we assume a large number of classical states, it is desirable that the projection onto classical states can be obtained through classical post-processing, which significantly reduces the workload of the quantum computer. One recent approach is the classical shadow method [27, 30]. However, local Pauli classical shadows rely on measurements in randomly chosen X , Y , and Z bases, whereas in our problem we only need projections onto the Z basis, since the determinants are defined in that basis. Furthermore, as the sample complexity of classical shadow shows, the required number of samples scales with the shadow norm, which grows exponentially with the number of qubits for the specific operators we seek to estimate. The dependence on the number of target observables is only logarithmic; in our setting, because the target observables are the determinant projections associated with the classical sector, this contribution scales as $\log N_c$. A full analysis of the sample complexity for Pauli-based classical shadows is derived in Section A 2. For larger systems the total sampling cost required to estimate all of these determinant projections can still become significant. Therefore, we propose a method optimized specifically for projections onto the Z -basis space, which we call *histogram-based overlap estimation*.

1. Histogram-based overlap estimation method

There are many possible approaches to overlap estimation; for example, recent work has considered time-series-based estimation of overlaps such as the Loschmidt amplitude [40].

To calculate the overlap, let

$$\alpha_s := \langle s | \phi_j^q \rangle, \quad \beta_s := \langle s | \chi \rangle, \quad (9)$$

where $|s\rangle$ represents a determinant and $|\phi_j^q\rangle$ a quantum basis state. Here, $|\chi\rangle$ is a batch consisting of the equal superposition of the classical states: $|\chi_k\rangle = \frac{1}{\sqrt{m}} \sum_{s \in S_k} |s\rangle$, where $m := |S_k|$ is the batch size and k indexes the equal-size batches. Thus, the amplitudes β_s are known and the number of batches is $B = \lceil N_c/m \rceil$. Define the interference states as

$$|\psi_R\rangle := \frac{1}{\sqrt{2}} (|\phi_j^q\rangle + |\chi\rangle), \quad |\psi_I\rangle := \frac{1}{\sqrt{2}} (|\phi_j^q\rangle + i |\chi\rangle), \quad (10)$$

and denote the computational-basis histograms by

$$p_q(s) := \mathbb{P}(s | \phi_j^q) = |\alpha_s|^2, \quad (11)$$

$$p_R(s) := |\langle s | \psi_R \rangle|^2, \quad (12)$$

$$p_I(s) := |\langle s | \psi_I \rangle|^2. \quad (13)$$

Here, note that $p_R(s)$ and $p_I(s)$ are not probabilities because $|\psi_R\rangle$ and $|\psi_I\rangle$ are not normalized states. Therefore, to obtain these quantities, we should renormalize the probabilities, as shown in Section IV. Then the per-string unbiased estimator for α_s is

$$\hat{\alpha}_s = \frac{[p_R(s) - \frac{1}{2}(p_q(s) + |\beta_s|^2)]}{\bar{\beta}_s} + i \frac{[p_I(s) - \frac{1}{2}(p_q(s) + |\beta_s|^2)]}{\bar{\beta}_s}. \quad (14)$$

where $\bar{\beta}_s$ denotes the complex conjugate of β_s , i.e., $\bar{\beta}_s = \beta_s^*$.

In general, the batch size m introduces a trade-off: larger m reduces the number of batches $B = \lceil N_c/m \rceil$ and hence the number of processing steps, but it also decreases $|\beta_s| = 1/\sqrt{m}$, making the estimator more sensitive to statistical noise and potentially increasing the estimation error. In our histogram-method simulations, we chose $m = 5000$ as a practical compromise, since it keeps B small enough to reduce runtime while maintaining $|\beta_s| = 1/\sqrt{5000} \approx 1.4 \times 10^{-2}$, which was empirically sufficient to retain chemical-accuracy-level performance.

2. From overlap to Hamiltonian matrix element

Using the property that the action of a Pauli string on a computational basis state yields another computational basis state with a new coefficient, we can obtain the Hamiltonian matrix element without additional quantum measurements, using only the elements of the overlap matrix. For a Hamiltonian decomposed as $H = \sum_{\gamma=1}^{n_H} h_\gamma P_\gamma$, we have

$$\mathcal{H}_{ij} = \langle \phi_i^c | H | \phi_j^q \rangle = \sum_{\gamma=1}^{n_H} h_\gamma \langle \phi_i^c | P_\gamma | \phi_j^q \rangle \quad (15)$$

$$= \sum_{\gamma=1}^{n_H} h_\gamma \theta_\gamma(s_i)^* \langle s_i \oplus b_\gamma | \phi_j^q \rangle, \quad (16)$$

where s_i represents a bit string of $|\phi_i^c\rangle$, $\theta_\gamma(s_i) = i^{m_\gamma} (-1)^{z_\gamma \cdot s_i}$, $z_\gamma \cdot s_i = \sum_k z_\gamma(k) s_k$, m_γ is the number of Y gate in the Pauli string P_γ , and P_γ , b_γ , and z_γ are defined as

$$P_\gamma = \bigotimes_{k=1}^{n_{\text{qubit}}} \sigma_{\gamma k}, \quad \sigma_{\gamma,k} \in I, X, Y, Z, \quad (17)$$

$$b_\gamma(k) = \begin{cases} 1, & \sigma_{\gamma k} \in \{X, Y\} \\ 0, & \text{otherwise} \end{cases}, \quad (18)$$

$$z_\gamma(k) = \begin{cases} 1, & \sigma_{\gamma k} \in \{Z, Y\} \\ 0, & \text{otherwise} \end{cases}. \quad (19)$$

Since $\langle s_i \oplus b_\gamma | \phi_j^q \rangle$ is an overlap between a quantum basis state and a determinant, we can extract this value from the overlap matrix, or simply set it to zero if the corresponding overlap element is absent. This method allows us to use measurements of the quantum state in the computational basis, which may already be available from measurements of the quantum–quantum block, to infer the values of all classical states and Hamiltonian matrix elements which have support on the quantum states.

3. Numerical benchmark of histogram-based estimation

To assess the practical performance of histogram-based overlap estimation, we numerically simulate sampled overlap matrices, post-process them into Hamiltonian matrices, and solve the resulting generalized eigenvalue problem with the locally optimal block preconditioned conjugate-gradient (LOBPCG) eigensolver [31–33]. Before turning to the larger benchmark set, we first compare histogram-based estimation with classical shadows on the H_4 system. Although H_4 is small, it already provides a clear illustration of the different noise sensitivities of the two methods. Figure 3(a) shows how the error of the reconstructed Hamiltonian matrix changes with the number of shots.

A direct comparison of raw shot counts requires some care, because a “shot” has a different meaning for the two methods. For classical shadows, one shot corresponds to a measurement of a Pauli operator for a given quantum state, whereas for histogram-based estimation one shot corresponds to a sample contributing to the computational-basis histogram of a given quantum state. For the full classical–quantum block, the total histogram shot count is therefore the per-histogram shot count multiplied by $N_q(1 + 2B)$, because each quantum basis state requires one reference histogram and $2B$ interference histograms. A fair comparison should therefore be based on the total shot complexity required to achieve a fixed error ϵ in an individual classical–quantum Hamiltonian matrix element \mathcal{H}_{ij} , as summarized in Table I. The full derivation of these sample complexities can be found in Section A. Both methods avoid an explicit linear dependence on N_c , the number of classical states, which is desirable in the CANOE regime where N_c is intentionally large. The key difference lies in the dependence on system size: classical shadows carry an exponential factor in the number of spin orbitals (equivalently qubits), whereas histogram-based estimation scales only linearly through the batching factor. This scaling difference explains the gap observed in Figure 3(a) and is consistent with the much milder behavior of classical shadows in smaller systems such as H_2 .

Figure 3(b) shows the same distinction at the level of determinant probabilities for H_4 : histogram-based estimation reproduces the ground-state distribution more faithfully than the classical-shadow approach.

We then benchmark histogram-based estimation across the molecular set H_4 , H_2O , NH_3 , HCN , CO_2 , and $COCl_2$,

Method	Total shots
Hadamard test [16]	$O\left(\frac{N_c N_q n_H \ \mathbf{H}\ _2^2}{\epsilon^2}\right)$
Classical shadow [27, 30]	$O\left(\frac{N_q \log(N_c) \ \mathbf{H}\ _1^2 3^{n_{\text{qubit}}}}{\epsilon^2}\right)$
Histogram-based estimation	$O\left(\frac{N_q(1+2B)m \ \mathbf{H}\ _1^2}{\epsilon^2} \log(2^{n_{\text{qubit}}} N_q(1+2B))\right)$

Table I. Sample complexity of the overlap-estimation methods for constructing the full classical–quantum (c - q) block. Here, N_c and N_q denote the numbers of classical and quantum states, respectively. m is the batch size. $B = \lceil N_c/m \rceil$ is the number of batches. n_H is the number of Pauli terms in the Hamiltonian. $\|\mathbf{H}\|_1$ and $\|\mathbf{H}\|_2$ are the corresponding coefficient one-norm and two-norm. ϵ is the target error in an individual classical–quantum Hamiltonian matrix element \mathcal{H}_{ij} . δ is the failure probability.

System	(so,e)	N_c	SHCI	N_q
H_4	(8,4)	10	36	4
H_2O	(14,10)	100	133	10
NH_3	(16,10)	1000	1259	10
HCN	(22,14)	10000	11712	64
CO_2	(30,22)	10000	46167	64
$COCl_2$	(56,48)	10000	98437	64

Table II. Benchmark molecules used to simulate histogram sampling. The notation (so, e) denotes the numbers of spin orbitals and electrons, respectively. N_c and N_q are the numbers of classical and quantum states, respectively. SHCI means the number of determinants of SHCI variational space.

using the simulation protocol described in Section IV. The benchmark systems are summarized in Table II. In Figure 3(c), the error in the classical–quantum block of the Hamiltonian matrix decreases toward zero as the number of shots increases, approximately following the expected $1/\sqrt{N_{\text{shot}}}$ scaling of the sampling model. The energy error in Figure 3(d) is governed by three factors: sampling error, truncated-subspace gap, and instability of the generalized eigensolver. First, the sampling error decreases systematically as the number of shots increases, as seen in Figure 3(c). Second, the dashed lines in Figure 3(d) show the truncation gap, namely the difference between the reference energy E_{true} and the infinite-shot-limit CANOE energy within the truncated subspace; if the truncated space does not represent the ground state sufficiently well, increasing the number of shots cannot overcome this floor. Third, the stability of the generalized eigensolver is particularly critical.

Figure 3(d) shows that the ground-state energy error does not decrease uniformly across systems. The reason is that the energy is obtained from the generalized eigenproblem, $E_0 = \frac{\mathbf{c}_0^\dagger \mathcal{H} \mathbf{c}_0}{\mathbf{c}_0^\dagger \mathcal{S} \mathbf{c}_0}$, rather than from an individual matrix element, where \mathbf{c}_0 is the lowest generalized-eigenvalue vector. As a result, the same level of sampling noise in the matrix elements of \mathcal{H} and \mathcal{S} can produce very different energy errors for different systems. This sensitivity

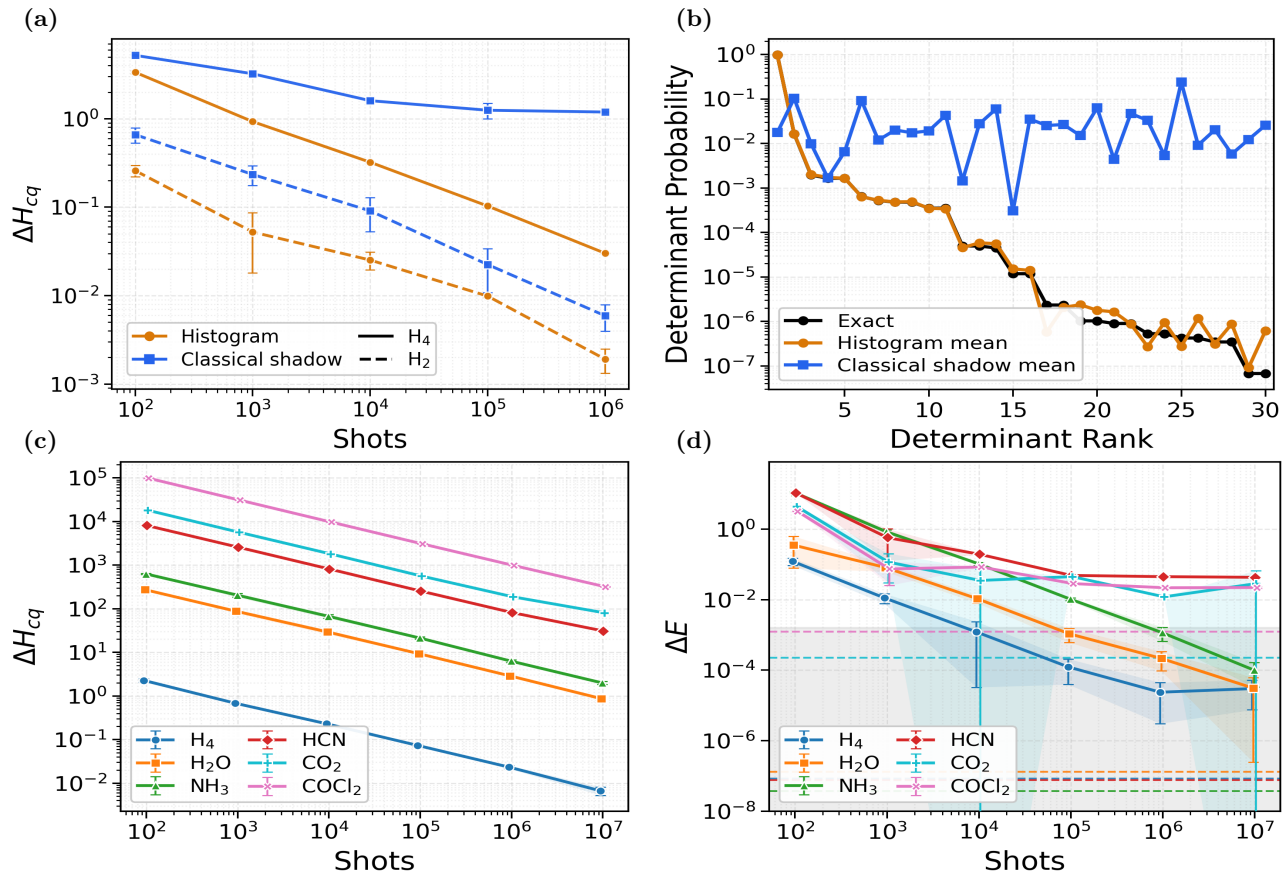


Figure 3. Numerical benchmark of histogram-based overlap estimation. **(a)**: Comparison between histogram-based and classical-shadow estimation for the Hamiltonian-matrix error ΔH as a function of the number of shots for H_4 (solid) and H_2 (dashed). The reference values are taken from the infinite-shot limit of the sampling simulation. For H_2 , we use $N_c = 2$ (the full SHCI space, used here to test sampling noise) and $N_q = 2$, while H_4 uses the same basis sizes as in Table II. **(b)**: Determinant probabilities versus determinant rank for H_4 , shown at 10^6 shots, comparing the histogram-based estimation and classical shadow against the “exact” result, where “exact” denotes the infinite-shot limit. **(c)**: Classical-quantum Hamiltonian-matrix error ΔH_{cq} obtained using the histogram-based estimation method as a function of the number of shots for the benchmark systems. The reference values are obtained from analytically computed Hamiltonian-matrix elements, corresponding to the infinite-shot limit. **(d)**: Ground-state energy error ΔE as a function of the number of shots for the same benchmark systems. The error is defined relative to the reference ground state energy, which is SHCI variational energy. The dashed lines indicate the gap between the SHCI variational energy and the infinite-shot-limit CANOE energy in the truncated subspace. The infinite-shot-limit ground-state energy is obtained by loading the exact truncated (H, S) matrices, Hermitizing them, solving $Hc = ESC$ with LOBPCG, deflation, and pseudo-inverse over a threshold sweep, and comparing the resulting solver outputs with E_{true} .

can become more pronounced when important components of \mathbf{c}_0 lie along small-eigenvalue directions of \mathcal{S} that are not well resolved at the current shot count; in that regime, near-linear dependencies can make the generalized eigensolver less stable and lead to plateaus or delayed convergence toward the infinite-shot limit. Therefore, the shot count required to reach chemical accuracy depends not only on the sample-complexity scaling, but also on the spectral conditioning of the truncated subspace for the specific system and the particular qualities of the generalized eigensolver used.

In the present numerical benchmarks, we introduced sampling noise only in the classical-quantum block. In a full quantum implementation, however, the quantum-quantum block would also need to be evaluated. One

direct option is the Hadamard test. Alternatively, if determinant amplitudes are reconstructed for each quantum basis state on a common determinant set and in a consistent phase convention, then both diagonal and off-diagonal quantum-quantum overlap and Hamiltonian matrix elements can in principle be assembled classically from those amplitudes, as shown in Section B. In practice, this reconstruction is exact only when the determinant set is sufficiently complete for the relevant Pauli-shifted support, so the Hadamard test remains a direct route when that condition is not met.

C. Generalized eigensolver for non-orthogonal basis

Since CANOE includes quantum basis states, the resulting basis is generally non-orthogonal and may even contain near-linear dependencies. This creates a numerical difficulty for iterative solvers of generalized eigenvalue problems, such as LOBPCG or Jacobi–Davidson, because they require repeated applications of S^{-1} or an equivalent stable factorization of the overlap matrix [31–33]. When S is nearly singular, standard Cholesky or LDL^T factorizations can become unstable [31, 32]. To avoid both the ill-conditioning of S and explicit diagonalization of the full large-scale problem, we exploit the block structure induced by the classical–quantum partition and work with the Schur complement of the quantum sector. This leads to two practical stabilization strategies: deflation of nearly dependent quantum directions and a pseudo-inverse-based preconditioner for LOBPCG.

With the classical states ordered first and the quantum states second, the overlap matrix can be written as

$$S = \begin{pmatrix} I & U \\ U^\dagger & M \end{pmatrix}, \quad (20)$$

where I is the classical–classical overlap block of size $N_c \times N_c$, U is the classical–quantum overlap block of size $N_c \times N_q$, and M is the quantum–quantum overlap block of size $N_q \times N_q$. The corresponding Schur complement is

$$S_{\text{schur}} = M - U^\dagger U. \quad (21)$$

We diagonalize this matrix as

$$S_{\text{schur}} = V \Lambda V^\dagger, \quad \Lambda = \text{diag}(\lambda_1, \dots, \lambda_{N_q}). \quad (22)$$

In the deflation approach, we discard eigenvectors whose eigenvalues satisfy $\lambda_i < \tau_{\text{rank}}$ and solve the problem in the reduced quantum subspace. Because N_q is typically small in our setting, explicit full diagonalization of S_{schur} is a reasonable way to implement this deflation step. In the pseudo-inverse approach, we construct S_{schur}^+ by inverting only the retained eigenvalues and use the resulting operator to build the LOBPCG preconditioner; in this case, the weak directions are flattened rather than deleted. The hybrid workflow used in practice is summarized in Algorithm 1.

Molecule	Analytic $1/ \lambda_{\min} $	Sampled $1/ \lambda_{\min} $
H ₄	∞	539.00 (± 264.03)
H ₂ O	∞	150.84 (± 21.71)
NH ₃	∞	47.39 (± 8.96)
HCN	7.48×10^{12}	8.33 (± 0.70)
CO ₂	5.82×10^{12}	2.69 (± 0.06)
COCl ₂	5.31×10^{12}	7.49 (± 0.21)

TABLE III. Comparison of the conditioning of analytic and sampled overlap matrices, measured by $1/|\lambda_{\min}|$. The sampled values denote the mean over the 10^7 -shot data.

Algorithm 1: Schur-complement hybrid solver

Require: $H = \begin{pmatrix} H_{cc} & H_{cq} \\ H_{qc} & H_{qq} \end{pmatrix}$, $S = \begin{pmatrix} I & U \\ U^\dagger & M \end{pmatrix}$

Require: stabilization mode $\in \{\text{Pseudo-inverse}, \text{Deflation}\}$, rank threshold τ_{rank} , initial block X_0

- 1: $S_{\text{schur}} \leftarrow M - U^\dagger U$
- 2: Diagonalize $S_{\text{schur}} = V \text{diag}(\lambda_1, \dots, \lambda_{N_q}) V^\dagger$
- 3: **if** mode = *Pseudo-inverse* **then**
- 4: $\mu_i \leftarrow \begin{cases} 1/\lambda_i, & \lambda_i > \tau_{\text{rank}}, \\ 0, & \lambda_i \leq \tau_{\text{rank}} \end{cases}$
- 5: $S_{\text{schur}}^+ \leftarrow V \text{diag}(\mu_1, \dots, \mu_{N_q}) V^\dagger$
- 6: $P_{\text{inv}} \approx \begin{pmatrix} I + U S_{\text{schur}}^+ U^\dagger & -U S_{\text{schur}}^+ \\ -S_{\text{schur}}^+ U^\dagger & S_{\text{schur}}^+ \end{pmatrix}$
- 7: $A_{\text{use}} \leftarrow H$, $B_{\text{use}} \leftarrow S$, $X_{\text{use}} \leftarrow X_0$
- 8: **end if**
- 9: **if** mode = *Deflation* **then**
- 10: $\mathcal{I}_+ \leftarrow \{i \mid \lambda_i > \tau_{\text{rank}}\}$, $V_+ \leftarrow V(:, \mathcal{I}_+)$
- 11: $U' \leftarrow U V_+$, $M' \leftarrow V_+^\dagger M V_+$
- 12: $H'_{cq} \leftarrow H_{cq} V_+$, $H'_{qc} \leftarrow V_+^\dagger H_{qc}$, $H'_{qq} \leftarrow V_+^\dagger H_{qq} V_+$
- 13: Build the reduced pair
- $A_{\text{use}} \leftarrow H' = \begin{pmatrix} H_{cc} & H'_{cq} \\ H'_{qc} & H'_{qq} \end{pmatrix}$
- $B_{\text{use}} \leftarrow S' = \begin{pmatrix} I & U' \\ (U')^\dagger & M' \end{pmatrix}$
- 14: $P_{\text{inv}} \approx (S')^{-1}$
- 15: **If** $X_0 = \begin{pmatrix} X_{0,c} \\ X_{0,q} \end{pmatrix}$, **set** $X_{\text{use}} \leftarrow \begin{pmatrix} X_{0,c} \\ V_+^\dagger X_{0,q} \end{pmatrix}$
- 16: **end if**

`lobpcg(A_use, X_use, B=B_use, M=P_inv, ...)`

For the results in Section II A, we used the hybrid solver summarized above. By contrast, for the results in Section II B, we used LOBPCG without additional deflation or pseudo-inverse regularization. In that setting, the sampled overlap matrices are perturbed by statistical noise away from the exact, highly linearly-dependent structure, which partially alleviates the ill-conditioning of S , as shown in Table III. In the sampled-noise regime considered here, truncating near-singular directions can distort the ground-state solution more than it improves the conditioning of the generalized eigenvalue problem. The appropriate treatment of the generalized eigenvalue problem should therefore be adapted to the noise level of the overlap matrix rather than fixed uniformly across all regimes.

To make this dependence explicit, we parameterized the noise level by the Frobenius norm $\|\Delta S\|_F$ of the overlap-matrix perturbation. We varied this quantity in two ways: first, by associating each finite-shot sampled

matrix with its corresponding $\|\Delta S\|_F$ value; and second, by constructing synthetic overlap matrices of the form $S(\alpha) = S + \alpha(S^{(N_0)} - S)$, where $S^{(N_0)}$ denotes a reference sampled matrix with $N_0 = 100000$, so that α continuously controls $\|\Delta S\|_F$. We then repeated the analysis across different Schur-complement thresholds and for three eigensolver variants: LOBPCG, LOBPCG with pseudo-inverse regularization, and LOBPCG with deflation. The resulting H_4 , H_2O , and COCl_2 benchmarks are shown in Figure 4.

Several important aspects of the eigensolver behavior can be seen in Figure 4. First, the eigensolvers respond differently to the Schur-complement threshold. In the sampled-matrix regime, the more aggressive threshold, $\tau_{\text{rank}} = 10^{-2}$, is more robust than $\tau_{\text{rank}} = 10^{-6}$ over a broad range of noise levels. This indicates that, for sampled matrices, it is often advantageous to remove weakly independent or poorly resolved quantum directions more strictly. One likely reason is that finite-shot noise can render the sampled overlap matrix indefinite, so the generalized eigenproblem is no longer strictly variational. In this regime, adding more noisy quantum directions does not necessarily improve the ground-state estimate; instead, truncating unstable directions can yield a better result, and in the extreme case a classical-only solve can outperform a noisy $(c + q)$ calculation.

Second, the figure shows that LOBPCG behaves continuously and stably across the sampled-noise regime. Among the tested methods, it often provides the most consistent performance as the noise level varies, and in many sampled cases it gives the smallest error. This is consistent with the observation that finite-shot noise shifts the smallest overlap modes away from zero in magnitude, thereby relieving the severe near-singularity of the analytic overlap matrix; see Table III, where the sampled matrices exhibit substantially better conditioning with respect to the smallest eigenvalue. As a consequence, LOBPCG can remain numerically stable on sampled matrices even though the corresponding infinite-shot-limit generalized eigenproblem is substantially harder.

Third, the infinite-shot-limit benchmark in Figure 4(c) shows that the quantum subspace can improve the ground-state energy when it is treated stably. For H_2O , the pseudo-inverse solver gives a smaller gap in the infinite-shot limit than the classical-only reference, demonstrating that the quantum directions contain useful variational information. However, this improvement is not fully recovered in the sampled case at the same threshold, showing that noise can mask the benefit of the quantum subspace.

Finally, the infinite-shot-limit benchmarks of H_4 and COCl_2 show that, even in the infinite-shot limit, where the variational principle should hold, the classical-only solution can still be the most accurate among the tested eigensolver outputs. This should not be interpreted as evidence that the quantum subspace is intrinsically unhelpful. Rather, it indicates that the current eigensolver cannot always resolve weakly independent quantum directions reliably in a nearly singular generalized eigenproblem.

The overall picture therefore involves two distinct mechanisms: in the sampled regime, noise can destroy the variational structure and make truncation beneficial; in the infinite-shot-limit regime, the main limitation is the numerical resolution of weakly independent quantum directions.

III. DISCUSSION

We introduced CANOE as a hybrid non-orthogonal eigensolver that combines a small number of quantum-prepared states with a much larger set of classical determinants. In the ideal hybrid-basis setting, these two sectors play complementary roles: the quantum states contribute variational directions that are difficult to reproduce classically, while the classical sector enlarges the representation space around them at comparatively low cost. To make this hybrid basis realizable, we introduced histogram-based overlap estimation for determinant-space (Z -basis) projections and used Schur-complement truncation to stabilize the resulting generalized eigenvalue problem. Within this framework, our numerical results reach chemical accuracy for the smaller benchmark systems H_4 , H_2O , and NH_3 after sampling noise, truncation gap, and generalized-eigensolver instability are taken into account. For the larger systems HCN , CO_2 , and COCl_2 , however, the present results indicate that further progress is still needed. In those cases, the remaining limitations come partly from the effect of sampling noise on the generalized eigensolver and partly from the finite numerical resolution of weakly independent directions even in the infinite-shot limit.

The main directions for further work are summarized below.

1. **Design of the hybrid basis.** The effectiveness of CANOE depends on both the quality and the quantity of the added basis states. On the quantum side, one must determine which ansatz is most effective for representing the ground state. We used Krylov states here because they provide a simple and well-defined construction, but once the initial state is fixed they are largely deterministic, being generated by Hamiltonian time evolution alone. This convenience does not guarantee that they are the most effective choice for ground-state representation, and more flexible ansätze may perform better [13, 41]. On the classical side, both the construction and the optimal size of the determinant sector are also nontrivial, and alternative classical ansätze based on sampled determinants may also be useful to explore [42]. As shown in Section C, different combinations of N_c and N_q can lead to very different ground-state errors. In the infinite-shot limit, enlarging the basis should not worsen the variational solution. In the sampled setting, however, adding more directions can instead degrade the result because noise can outweigh the gain in expressivity and the strict

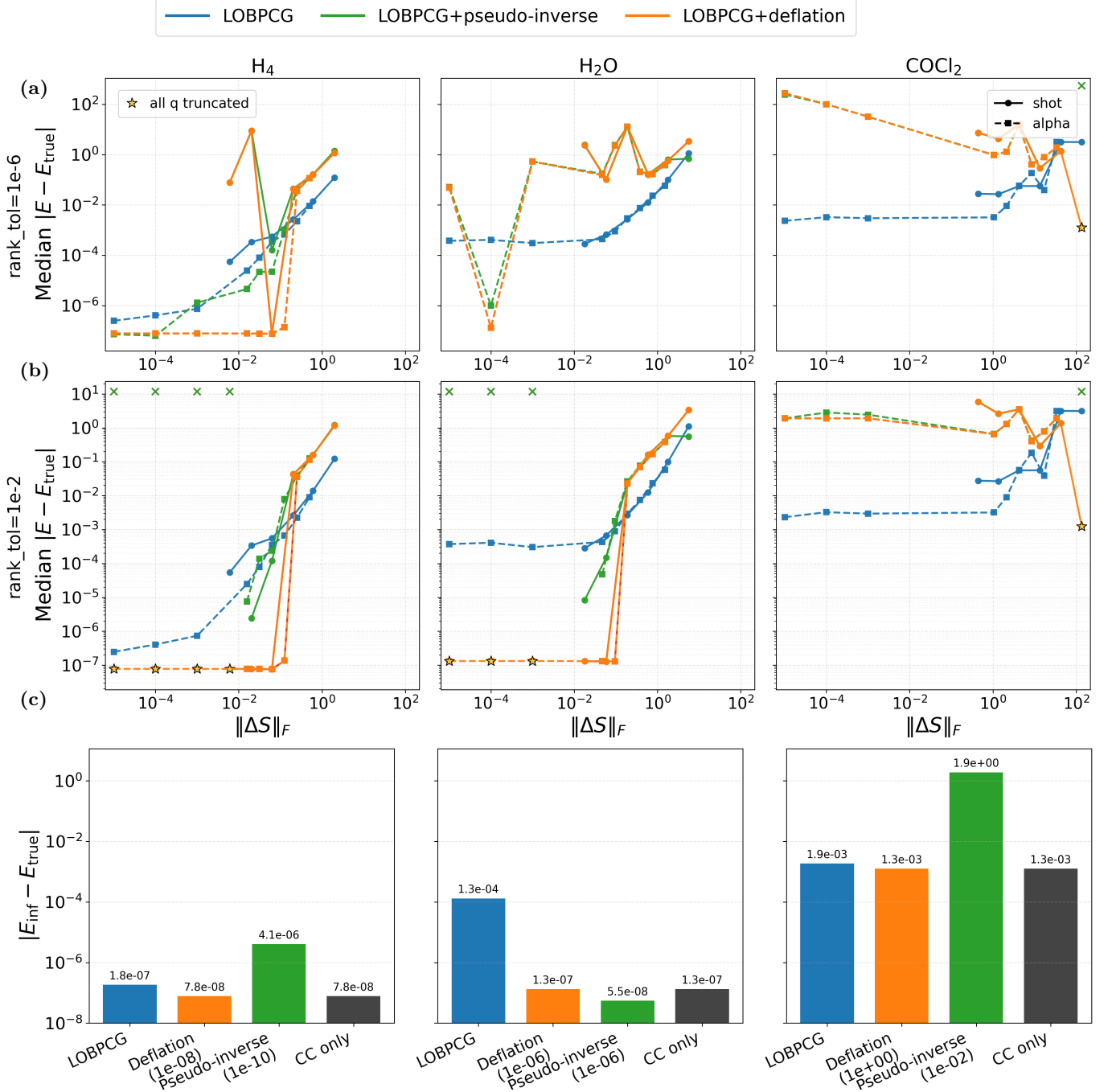


Figure 4. Benchmark of eigensolver performance versus overlap-matrix noise for H_4 , H_2O , and $COCl_2$. Columns correspond to the three molecular systems. (a) and (b) show the median ground-state energy error, $|E - E_{true}|$, as a function of $\|\Delta S\|_F$ for $\tau_{rank} = 10^{-6}$ and 10^{-2} , respectively, where E denotes the ground-state energy estimated from the noisy matrices. In these two rows, solid curves denote the sampled-matrix benchmark and dashed curves denote the synthetic α -noise benchmark. Blue, green, and orange denote LOBPCG, LOBPCG+pseudo-inverse, and LOBPCG+deflation, respectively. Green “x” markers indicate cases in which the pseudo-inverse solver failed to return a result, and star-shaped markers indicate cases in which all quantum directions were truncated so that only the classical subspace remained. (c) shows the corresponding infinite-shot-limit benchmarks, $E_{inf} - E_{true}$, together with the classical-classical only (CC-only) reference for each system shown in black. Values closer to zero indicate better agreement with the SHCI variational reference energy.

variational character of the generalized eigenproblem may be lost.

2. Plateau behavior and robust generalized eigensolvers. The plateau behavior observed in the sampled-energy benchmarks is not yet fully understood. In our numerical tests, it appears to be related to the weight of the ground state on the nearly singular eigenvectors of the overlap matrix. This provides a useful consistency check, but it does not yet explain the plateau quantitatively, in particular its onset and magnitude across different systems. More generally, the eigensolver remains a key bottleneck for CANOE. In practice, it may fail to resolve subtle but physically meaningful differences between weakly independent quantum directions, thereby suppressing their contribution to the final solution. At the same time, sampled overlap matrices can become indefinite, so the noisy problem may leave the strictly variational regime. A more detailed analysis of how overlap-matrix noise propagates to the final energy error is therefore still needed, together with improved strategies that either enhance the numerical resolution of the generalized eigensolver in nearly singular hybrid subspaces or remain reliable when the sampled matrices are noisy and indefinite. Generalized eigenvalue solvers specialized for noisy matrices may solve some of these issues [43].

On the measurement side, it is also worth exploring whether amplitude-estimation-based strategies, including recent Bayesian iterative variants, can be adapted to the overlap-estimation problem to further reduce sampling cost, although integrating such methods with the present histogram protocol remains future work [44].

If progress can be made on the two issues above, then a more meaningful comparison with other early fault-tolerant quantum algorithms becomes possible. Under the assumption that the plateau behavior can be mitigated by improved treatment of the generalized eigensolver, the extrapolation in Section E suggests that CANOE could still reach chemical accuracy for larger systems at finite sampling cost. Our current extrapolation gives a per-histogram shot count on the order of 10^8 at the 100-qubit scale, which corresponds to a total classical–quantum-block sampling cost closer to 10^{10} shots as the total shots for the energy. This places CANOE in a regime where comparison with VQE is most naturally made through total sampling cost. Early resource estimates for strongly correlated transition-metal chemistry gave VQE sampling costs as large as $\sim 10^{13}$ shots per energy evaluation [45], while later factorized measurement strategies reduce common bounds substantially, in some cases by about three orders of magnitude [46]; however, the total VQE cost still depends strongly on the ansatz, measurement scheme, and number of optimization steps. By contrast, comparison with QPE and related fault-tolerant quantum-simulation approaches is more naturally made through coherent circuit cost. Recent local-control formulations also suggest that phase-estimation-style algorithms can be adapted

toward shallower coherent implementations [47, 48]. In Section F, a naive first-order Trotter estimate with Jordan–Wigner decomposition gives a CANOE state-preparation depth of order 10^{11} for a 100-qubit-scale system. Canonical Trotterized FeMoco QPE estimates were on the order of 10^{14} – 10^{15} logical non-Clifford gates [49], whereas more optimized qubitization and tensor-factorization analyses substantially reduce the fault-tolerant cost, to around 10^9 gates [50]. These resource measures are not directly equivalent to our depth estimate, but they suggest that CANOE may occupy an intermediate regime between measurement-heavy variational methods and fully coherent phase-estimation approaches.

From another perspective, one can treat CANOE as a way to push for a wavefunction ansatz that is (under sufficient sampling conditions) strictly better than what can be achieved on a classical or a quantum computer alone. Recent demonstrations of Fermi–Hubbard dynamics on a 72-qubit quantum processor [51] demonstrate that time-evolution, even with Trotterization, is becoming possible. The states prepared in Ref. [51] could be used to create the necessary quantum states. On the other side, recent advances in selected configuration interaction methods have demonstrated compact, expressive determinant expansions that can provide quality approximations of the ground state [42]. CANOE could use these state-of-the-art determinant expansions as the classical states. Putting them together, with a sufficiently robust generalized eigensolver and sufficient shots, would result in an estimate of the ground state that is better than either the classical or quantum computer by themselves.

IV. METHODS

Here, we summarize the additional implementation details used in our numerical benchmarks, including the construction of the hybrid basis, the overlap-estimation workflows, and the generalized eigensolver.

A. Hybrid-Basis Construction

The construction of the classical and quantum basis states is described in Section II A; here we note only the additional setup details used in practice. The Hamiltonian is constructed in the selected heat-bath configuration interaction (SHCI) variational space. The underlying determinant set is generated using a SHCI procedure [38] with variational selection threshold $\epsilon_{\text{var}} = 5 \times 10^{-5}$. This yields a compact yet near-converged approximation to the full configuration interaction (FCI) space, enabling simulations of moderately large correlated systems. From this SHCI-selected determinant set, we retain the leading N_c determinants ranked by variational coefficient. Within the same SHCI space, the quantum basis states are constructed to capture low-energy correlations. For the chromium numerical experiment in Section II A, the

SHCI variational space contains 1.4×10^6 determinants, from which we construct classical basis subsets of varying size N_c , together with up to 64 Krylov states as quantum basis states.

B. Overlap estimation methods

1. Practical implementation of histogram-based estimation

Because the interference states $|\psi_R\rangle$ and $|\psi_I\rangle$ are not normalized, they cannot be prepared directly with a unitary circuit. Instead, we introduce an ancilla qubit and prepare

$$|\Psi\rangle := \frac{1}{\sqrt{2}} \left(|0\rangle |\phi_j^q\rangle + |1\rangle |\chi\rangle \right). \quad (23)$$

If the ancilla is measured in the X basis, implemented by a final Hadamard gate followed by computational-basis readout, and the remaining qubits are measured in the Z basis, then the joint histogram for determinant s is

$$J_R(s) := \mathbb{P}(+X, s) = \frac{1}{4} |\alpha_s + \beta_s|^2, \quad (24)$$

where $\alpha_s = \langle s | \phi_j^q \rangle$ and $\beta_s = \langle s | \chi \rangle$. Replacing the final Hadamard by HS^\dagger , i.e., measuring the ancilla in the Y basis, gives

$$J_I(s) := \mathbb{P}(+Y, s) = \frac{1}{4} |\alpha_s + i\beta_s|^2. \quad (25)$$

These histograms satisfy

$$p_R(s) = 2J_R(s), \quad p_I(s) = 2J_I(s), \quad (26)$$

so the estimator introduced in Section II can be evaluated directly from the measured joint histograms without any additional normalization of $|\psi_R\rangle$ and $|\psi_I\rangle$. A schematic circuit is shown in Figure 5.

In the numerical simulations reported here, we benchmarked histogram-based estimation across the molecular set H_4 , H_2O , NH_3 , HCN , CO_2 , and COCl_2 . For each system, we first constructed an SHCI variational space with selection threshold $\epsilon_{\text{var}} = 10^{-5}$ and used the resulting variational energy as the reference ground-state energy within our numerical setup. This reference is not the exact FCI energy, but it is sufficiently accurate for our benchmarking purposes. The same SHCI space defines the determinant pool from which the CANOE basis is assembled. In the intended CANOE regime, we retain a large classical sector and a comparatively small number of quantum states, both defined within this SHCI space. To form the sampled overlap matrices, we use the identity for the classical–classical block and analytically computed values for the quantum–quantum block; in an actual quantum implementation, the latter would be obtained with the Hadamard test. Sampling noise is introduced only in the classical–quantum block, while the quantum–quantum block is kept at its analytically computed value.

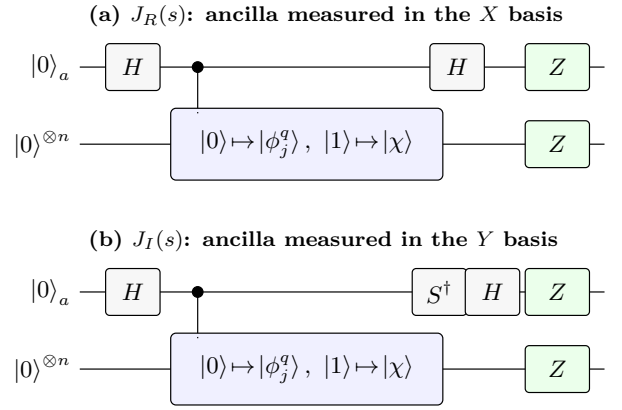


Figure 5. Ancilla-assisted implementation of histogram-based overlap estimation. The ancilla-assisted preparation yields $|\Psi\rangle = \frac{1}{\sqrt{2}}(|0\rangle |\phi_j^q\rangle + |1\rangle |\chi\rangle)$. Measuring the ancilla in the X or Y basis and the system register in the computational basis gives the joint histograms J_R and J_I , respectively.

2. Practical implementation of classical shadow

For local Pauli classical shadows, each quantum basis state is measured repeatedly in randomly chosen single-qubit Pauli bases. Each shot records both the basis choices and the corresponding bit string, from which a classical-shadow snapshot is reconstructed. To recover the complex overlap with a classical determinant $|\phi_i^c\rangle$, we define the off-diagonal observables

$$\begin{aligned} O_i^{(X)} &:= |0^n\rangle \langle \phi_i^c| + |\phi_i^c\rangle \langle 0^n|, \\ O_i^{(Y)} &:= i(|0^n\rangle \langle \phi_i^c| - |\phi_i^c\rangle \langle 0^n|), \end{aligned}$$

and prepare the reference-interference state

$$|\psi_R\rangle = \frac{|\phi_j^q\rangle + |0^n\rangle}{\sqrt{2}}.$$

Their expectation values give the real and imaginary parts of the overlap,

$$\begin{aligned} \langle \psi_R | O_i^{(X)} | \psi_R \rangle &= \text{Re} \langle \phi_i^c | \phi_j^q \rangle, \\ \langle \psi_R | O_i^{(Y)} | \psi_R \rangle &= \text{Im} \langle \phi_i^c | \phi_j^q \rangle. \end{aligned}$$

In practice, this means that for each quantum basis state one must estimate a pair of observables for every classical determinant, i.e., $2N_c$ target observables in total. In our numerical implementation, we used the code from the ShadowGrouping reference [29], adjusted its parameters to implement randomized classical shadows, and interfaced it with our own routines to project the sampled states onto determinants in the SHCI space. More generally, software support for randomized-measurement workflows is also available through packages such as RandomMeas.jl [52].

C. Practical implementation of the generalized eigensolver

For the numerical simulations in this work, the LOBPCG iterations were carried out with the implementation provided by `scipy.sparse.linalg.lobpcg`. This library routine was used within our own Schur-complement-based solver workflow to treat the generalized eigenvalue problem in the CANOE basis. For the sampled matrices, we use LOBPCG alone in a uniform manner across all systems. At moderate shot counts, the sampling noise effectively regularizes the ill-conditioning of \mathcal{S} , so additional deflation or pseudo-inverse stabilization is not yet necessary. As the sampling error is reduced and the calculation enters the high-accuracy regime, however, the underlying near-linear dependencies re-emerge, and the

same deflation and pseudo-inverse treatment used for the infinite-shot limit becomes necessary. Its effect on the benchmarks is discussed in Section II.

ACKNOWLEDGMENTS

We thank Preetham Tikkireddi for useful discussions. The authors acknowledge the use of OpenAI’s ChatGPT and Codex for editorial assistance in organizing and refining the presentation of this manuscript. This material is based upon work supported by NSF Award No. 2016136 for the QLCI center Hybrid Quantum Architectures and Networks and the U.S. Department of Energy Office of Science National Quantum Information Science Research Centers as part of the Q-NEXT center.

Appendix A: Sample-complexity derivations for overlap-estimation methods

1. Hadamard test

To estimate an overlap or Hamiltonian matrix element between two quantum basis states $|\phi_i^q\rangle$ and $|\phi_j^q\rangle$, the Hadamard-test circuit creates an ancilla-mediated interference state. Following Ref. [30], the final state can be written as

$$|\phi_{ij}^{\text{end}}\rangle = \frac{1}{\sqrt{2}} (|\phi_i^q\rangle |+\rangle + e^{i\theta} |\phi_j^q\rangle |-\rangle). \quad (\text{A1})$$

Measuring $I \otimes Z$ on this state yields the overlap matrix element. For $\theta = 0$,

$$\langle \phi_{ij}^{\text{end}} | I \otimes Z | \phi_{ij}^{\text{end}} \rangle = \text{Re}(\langle \phi_i^q | \phi_j^q \rangle) = \text{Re}(S_{ij}), \quad (\text{A2})$$

while for $\theta = \pi/2$,

$$\langle \phi_{ij}^{\text{end}} | I \otimes Z | \phi_{ij}^{\text{end}} \rangle = \text{Im}(\langle \phi_i^q | \phi_j^q \rangle) = \text{Im}(S_{ij}). \quad (\text{A3})$$

Let

$$H = \sum_{k=1}^{n_H} h_k P_k. \quad (\text{A4})$$

Then the same construction gives the Hamiltonian matrix element. For $\theta = 0$,

$$\langle \phi_{ij}^{\text{end}} | H \otimes Z | \phi_{ij}^{\text{end}} \rangle = \text{Re}(\langle \phi_i^q | H | \phi_j^q \rangle) = \text{Re}(H_{ij}), \quad (\text{A5})$$

while for $\theta = \pi/2$,

$$\langle \phi_{ij}^{\text{end}} | H \otimes Z | \phi_{ij}^{\text{end}} \rangle = \text{Im}(\langle \phi_i^q | H | \phi_j^q \rangle) = \text{Im}(H_{ij}). \quad (\text{A6})$$

Let U_{end} denote the circuit that prepares $|\phi_{ij}^{\text{end}}\rangle$. Using the Pauli decomposition, the real-part estimator can be written as

$$\langle \phi_{ij}^{\text{end}} | H \otimes Z | \phi_{ij}^{\text{end}} \rangle = \sum_{k=1}^{n_H} h_k \langle 0 | U_{\text{end}}^\dagger (P_k \otimes Z) U_{\text{end}} | 0 \rangle. \quad (\text{A7})$$

Assume that the n_H Pauli terms are measured independently and that each term is assigned the same number of shots n_{meas} . Let $X \in \{-1, +1\}$ denote the outcome of a single Pauli measurement, with probabilities p and $q = 1 - p$. Then

$$\mu = \mathbb{E}[X] = p - (1 - p) = 2p - 1, \quad (\text{A8})$$

and the variance of the estimated probability is

$$\text{Var}(\hat{p}) = \frac{pq}{n_{\text{meas}}}. \quad (\text{A9})$$

Therefore, the variance of the sample mean of X satisfies

$$\text{Var}(\hat{X}) = 4 \text{Var}(\hat{p}) = \frac{4pq}{n_{\text{meas}}} \leq \frac{1}{n_{\text{meas}}}. \quad (\text{A10})$$

The variance of the estimator for $\langle \phi_{ij}^{\text{end}} | H \otimes Z | \phi_{ij}^{\text{end}} \rangle$ is then bounded by

$$\text{Var} \leq \sum_{k=1}^{n_H} h_k^2 \text{Var}(\hat{\mu}_k) \leq \sum_{k=1}^{n_H} \frac{h_k^2}{n_{\text{meas}}} = \frac{\|\mathbf{H}\|_2^2}{n_{\text{meas}}}, \quad (\text{A11})$$

where n_{meas} is the number of shots per Pauli observable.

If the target standard error for $\text{Re}(H_{ij})$ is ϵ , it is sufficient to choose

$$n_{\text{meas}} \geq \frac{\|\mathbf{H}\|_2^2}{\epsilon^2}. \quad (\text{A12})$$

Because the n_H observables are measured separately, the total number of shots sufficient to estimate one real-valued matrix element is

$$n_{\text{shot}}^{\text{Re}(H_{ij})} \geq n_H n_{\text{meas}} \geq \frac{n_H \|\mathbf{H}\|_2^2}{\epsilon^2}. \quad (\text{A13})$$

Consequently, the number of shots required for the full $N_c \times N_q$ classical-quantum block of the Hamiltonian matrix is

$$\boxed{n_{\text{block}_{cq}} \geq 2N_c N_q n_{\text{shot}}^{\text{Re}(H_{ij})} \geq \frac{2N_c N_q n_H \|\mathbf{H}\|_2^2}{\epsilon^2}}, \quad (\text{A14})$$

where the factor of 2 accounts for measuring both the real and imaginary parts.

2. Classical shadow

To recover the complex overlap $\langle \phi_i^c | \phi_j^q \rangle$ with classical shadows, it is convenient to introduce observables whose expectation values directly return its real and imaginary parts with respect to the reference string $|0^n\rangle$. For classical-shadow estimation, define the off-diagonal observables

$$O_i^{(X)} := |0^n\rangle \langle \phi_i^c| + |\phi_i^c\rangle \langle 0^n|, \quad (\text{A15})$$

$$O_i^{(Y)} := i(|0^n\rangle \langle \phi_i^c| - |\phi_i^c\rangle \langle 0^n|). \quad (\text{A16})$$

Using the same reference-interference construction, for a target quantum basis state $|\phi_j^q\rangle$, consider the state

$$|\psi_R\rangle = \frac{|\phi_j^q\rangle + |0^n\rangle}{\sqrt{2}}, \quad (\text{A17})$$

the expectation values of these observables satisfy

$$\langle \psi_R | O_i^{(X)} | \psi_R \rangle = \frac{1}{2} (\langle \phi_j^q | \phi_i^c \rangle + \langle \phi_i^c | \phi_j^q \rangle) = \text{Re} \langle \phi_i^c | \phi_j^q \rangle, \quad (\text{A18})$$

$$\langle \psi_R | O_i^{(Y)} | \psi_R \rangle = \frac{1}{2} (-i \langle \phi_j^q | \phi_i^c \rangle + i \langle \phi_i^c | \phi_j^q \rangle) = \text{Im} \langle \phi_i^c | \phi_j^q \rangle. \quad (\text{A19})$$

Therefore, by preparing the corresponding state $|\psi_R\rangle$ for each quantum basis state $|\phi_j^q\rangle$ and estimating $O_i^{(X)}$ and $O_i^{(Y)}$ with classical shadows, one can reconstruct the complex overlap element S_{ij} .

For each quantum state, this requires estimating the two observables $O_i^{(X)}$ and $O_i^{(Y)}$ for every classical basis state $|\phi_i^c\rangle$, so the total number of target observables is $M = 2N_c$. Using the standard classical-shadow bound for simultaneously estimating M observables, the required number of shots is

$$n_{\text{shot}} = KN = 2 \log \left(\frac{2M}{\delta} \right) \times \frac{34}{\epsilon^2} \max_{1 \leq i \leq M} \|O_i\|_{\text{shadow}}^2. \quad (\text{A20})$$

In the present case, the relevant observables are off-diagonal many-body operators. For local Pauli classical shadows, a worst-case bound is

$$\|O_i\|_{\text{shadow}}^2 = \mathcal{O}(3^{n_{\text{qubit}}}).$$

Using $M = 2N_c$, this gives the sufficient bound for the overlap estimation of one quantum basis state $|\phi_j^q\rangle$, where η is the target overlap error. Since H_{ij} is reconstructed from the sampled overlaps through Eq. (16), the induced error satisfies the sufficient bound

$$|\hat{H}_{ij} - H_{ij}| \leq \|\mathbf{H}\|_1 \eta. \quad (\text{A21})$$

Therefore, to achieve a target error ϵ in $\text{Re}(H_{ij})$, it is sufficient to choose

$$n_{\text{shot}}^{\text{Re}(H_{ij})} \geq 68 \cdot 3^{n_{\text{qubit}}} \frac{\|\mathbf{H}\|_1^2 \log(4N_c/\delta)}{\epsilon^2}. \quad (\text{A22})$$

Across all N_q quantum basis states, the full classical–quantum block then requires

$$n_{\text{block}_{c_q}} \geq N_q n_{\text{shot}}^{\text{Re}(H_{ij})} \geq 68 N_q 3^{n_{\text{qubit}}} \frac{\|\mathbf{H}\|_1^2 \log(4N_c/\delta)}{\epsilon^2}, \quad (\text{A23})$$

Note that this estimate assumes local Pauli classical shadows; other shadow protocols may exhibit different sample-complexity scalings. Table II lists only the corresponding big- O scaling.

3. Histogram-based estimation

Fix one quantum basis state $|\phi_j^q\rangle$. Partition the selected classical strings into B disjoint batches of size m , so $B = \lceil N_c/m \rceil$. For batch k , define the reference state

$$|\chi_k\rangle = \frac{1}{\sqrt{m}} \sum_{s \in S_k} |s\rangle, \quad (\text{A24})$$

so that

$$\beta_s \equiv \langle s | \chi_k \rangle = \begin{cases} 1/\sqrt{m}, & s \in S_k, \\ 0, & s \notin S_k. \end{cases} \quad (\text{A25})$$

For each quantum basis state, one measures one reference histogram and $2B$ interference histograms, giving $1 + 2B$ histograms in total. Over all N_q quantum states, this becomes $N_q(1 + 2B)$ histograms. Let n_{meas} denote the number of shots per histogram. Here n_{meas} denotes the shots used to estimate a single histogram, whereas n_{shot} below denotes the total shot count summed over all histograms and all quantum basis states.

a. Estimator. For $s \in S_k$, where $\beta_s = 1/\sqrt{m}$, the estimator is

$$\hat{\alpha}_s = \frac{\hat{p}_R^{(k)}(s) - \frac{1}{2}(\hat{p}_q(s) + |\beta_s|^2) + i[\hat{p}_I^{(k)}(s) - \frac{1}{2}(\hat{p}_q(s) + |\beta_s|^2)]}{\beta_s} \quad (\text{A26})$$

$$= \sqrt{m} \left[\hat{p}_R^{(k)}(s) - \frac{1}{2}(\hat{p}_q(s) + \frac{1}{m}) \right] + i\sqrt{m} \left[\hat{p}_I^{(k)}(s) - \frac{1}{2}(\hat{p}_q(s) + \frac{1}{m}) \right]. \quad (\text{A27})$$

b. Hoeffding bounds for histogram errors. For a full histogram on n_{qubit} qubits, there are $2^{n_{\text{qubit}}}$ computational-basis outcomes. Applying Hoeffding's inequality to each bin and a union bound over all bins gives

$$\mathbb{P}\left(\max_s |\hat{p}(s) - p(s)| \geq \epsilon\right) \leq 2 \cdot 2^{n_{\text{qubit}}} e^{-2n_{\text{meas}}\epsilon^2}. \quad (\text{A28})$$

Applying a union bound over the N_q reference histograms and the $N_q B$ real and imaginary interference histograms gives

$$\mathbb{P}\left(\max\{|\Delta p_q|, |\Delta p_R|, |\Delta p_I|\} \geq \epsilon\right) \leq 2 \cdot 2^{n_{\text{qubit}}} N_q(1 + 2B) e^{-2n_{\text{meas}}\epsilon^2}. \quad (\text{A29})$$

Thus, with confidence $1 - \delta$,

$$\epsilon \leq \sqrt{\frac{1}{2n_{\text{meas}}} \ln \frac{2 \cdot 2^{n_{\text{qubit}}} N_q(1 + 2B)}{\delta}}. \quad (\text{A30})$$

c. *Propagation to amplitude error.* If $|\Delta p_q| \leq \varepsilon$, $|\Delta p_R| \leq \varepsilon$, and $|\Delta p_I| \leq \varepsilon$, then for $s \in S_k$ one has

$$|\operatorname{Re}(\hat{\alpha}_s - \alpha_s)| = \frac{|(\Delta p_R) - \frac{1}{2}(\Delta p_q)|}{|\beta_s|} \leq \frac{3}{2}\sqrt{m}\varepsilon, \quad (\text{A31})$$

$$|\operatorname{Im}(\hat{\alpha}_s - \alpha_s)| = \frac{|(\Delta p_I) - \frac{1}{2}(\Delta p_q)|}{|\beta_s|} \leq \frac{3}{2}\sqrt{m}\varepsilon. \quad (\text{A32})$$

Therefore,

$$|\hat{\alpha}_s - \alpha_s| \leq \sqrt{2} \cdot \frac{3}{2}\sqrt{m}\varepsilon \leq \frac{3}{2}\sqrt{\frac{m}{n_{\text{meas}}} \ln \frac{2 \cdot 2^{n_{\text{qubit}}} N_q (1 + 2B)}{\delta}}. \quad (\text{A33})$$

d. *Per-amplitude target accuracy.* Demanding $|\hat{\alpha}_s - \alpha_s| \leq \eta$ uniformly over all strings and all quantum states with confidence $1 - \delta$ is guaranteed if

$$n_{\text{meas}} \geq \frac{9}{4} \frac{m}{\eta^2} \ln \frac{2 \cdot 2^{n_{\text{qubit}}} N_q (1 + 2B)}{\delta}. \quad (\text{A34})$$

e. *Total shot count.* Each quantum basis state requires $(1 + 2B)n_{\text{meas}}$ shots, so over all N_q quantum states

$$n_{\text{shot}} \geq N_q (1 + 2B) \frac{9}{4} \frac{m}{\eta^2} \ln \left(\frac{2 \cdot 2^{n_{\text{qubit}}} N_q (1 + 2B)}{\delta} \right). \quad (\text{A35})$$

Finally, since the error in $\langle s | H | \phi_j^q \rangle = \sum_{\gamma} h_{\gamma} (-i)^{|Y_{\gamma}|} (-1)^{s \cdot p_{\gamma}} \alpha_{s \oplus b_{\gamma}}$ scales as $\|\mathbf{H}\|_1 \eta$, setting $\epsilon = \|\mathbf{H}\|_1 \eta$ gives

$$\boxed{n_{\text{shot}} \geq N_q (1 + 2B) \frac{9}{4} \frac{m \|\mathbf{H}\|_1^2}{\epsilon^2} \ln \left(\frac{2 \cdot 2^{n_{\text{qubit}}} N_q (1 + 2B)}{\delta} \right)}. \quad (\text{A36})$$

Table II lists only the corresponding big- O scaling.

These sample-complexity bounds quantify the measurement effort required to control the reconstruction error of the sampled overlap and Hamiltonian matrices. A convenient perturbative regime is

$$\|\delta H\|_2 + |E_0| \|\delta S\|_2 \ll \Delta_{\text{gen}}, \quad \Delta_{\text{gen}} := \min_{k \neq 0} |E_k - E_0|, \quad (\text{A37})$$

where E_k are the exact generalized eigenvalues. In this regime, first-order perturbation theory can be used to estimate the induced ground-state energy error. Bounds on the sampled errors in H and S then translate directly into a bound on the energy shift through the first-order relation

$$\delta E^{(1)} = v_0^\dagger (\delta H - E_0 \delta S) v_0.$$

Coherent hardware noise or correlated readout errors are not included in this statistical model; such effects can introduce a bias term and modify the prefactor of the energy-error bound, but do not change the leading $n_{\text{shot}}^{-1/2}$ scaling of the sampling error to first order.

Appendix B: Reconstructing the quantum–quantum block from determinant overlaps

Let

$$\alpha_s^{(j)} := \langle s | \phi_j^q \rangle, \quad \alpha_s^{(k)} := \langle s | \phi_k^q \rangle, \quad (\text{B1})$$

denote the determinant amplitudes of two quantum basis states $|\phi_j^q\rangle$ and $|\phi_k^q\rangle$. If these amplitudes are reconstructed on a common determinant set \mathcal{D} and with a consistent phase convention, then the quantum–quantum overlap element can be written as

$$\mathcal{S}_{jk} = \langle \phi_j^q | \phi_k^q \rangle = \sum_s \overline{\alpha_s^{(j)}} \alpha_s^{(k)}. \quad (\text{B2})$$

Therefore, when the determinant amplitudes are known on the full support of the two states, the overlap block \mathcal{S}_{qq} can be assembled classically. If only the amplitudes on a restricted set \mathcal{D} are available, the corresponding truncated approximation is

$$\tilde{\mathcal{S}}_{jk}^{(\mathcal{D})} = \sum_{s \in \mathcal{D}} \overline{\alpha_s^{(j)}} \alpha_s^{(k)}. \quad (\text{B3})$$

In general, $\tilde{\mathcal{S}}_{jk}^{(\mathcal{D})}$ is not exact, since contributions from determinants outside \mathcal{D} are omitted. The special case $j = k$ becomes exact only when \mathcal{D} is taken to be the full computational-basis support of the same quantum state, so that the sum reduces to the full histogram normalization $\sum_s |\alpha_s^{(j)}|^2 = 1$. For a restricted selected determinant set, even the diagonal case remains a truncated approximation.

For the Hamiltonian block, using the Pauli decomposition

$$H = \sum_{\gamma=1}^{n_H} h_\gamma P_\gamma, \quad (\text{B4})$$

and the computational-basis action

$$P_\gamma |s\rangle = \theta_\gamma(s) |s \oplus b_\gamma\rangle, \quad (\text{B5})$$

one obtains

$$\mathcal{H}_{jk} = \langle \phi_j^q | H | \phi_k^q \rangle = \sum_{\gamma=1}^{n_H} h_\gamma \langle \phi_j^q | P_\gamma | \phi_k^q \rangle = \sum_{\gamma=1}^{n_H} h_\gamma \sum_s \overline{\alpha_s^{(j)}} \theta_\gamma(s) \alpha_{s \oplus b_\gamma}^{(k)}. \quad (\text{B6})$$

This shows that off-diagonal quantum–quantum Hamiltonian elements are also recoverable in principle from determinant amplitudes, not only the diagonal case $j = k$.

If amplitudes are available only on a restricted determinant set \mathcal{D} , then for each Pauli term one must also require the shifted string $s \oplus b_\gamma$ to remain inside \mathcal{D} . Defining

$$\mathcal{D}_\gamma := \{ s \in \mathcal{D} \mid s \oplus b_\gamma \in \mathcal{D} \}, \quad (\text{B7})$$

the corresponding truncated reconstruction is

$$\tilde{\mathcal{H}}_{jk}^{(\mathcal{D})} = \sum_{\gamma=1}^{n_H} h_\gamma \sum_{s \in \mathcal{D}_\gamma} \overline{\alpha_s^{(j)}} \theta_\gamma(s) \alpha_{s \oplus b_\gamma}^{(k)}. \quad (\text{B8})$$

Hence the reconstruction is exact only when the chosen determinant set is sufficiently complete for all Pauli-shifted amplitudes that contribute appreciably to Eq. (B6). When that condition is not satisfied, direct interference-based measurements such as the Hadamard test remain a more straightforward way to evaluate the quantum–quantum block.

Appendix C: Dependence of sampled CANOE simulations on N_c and N_q

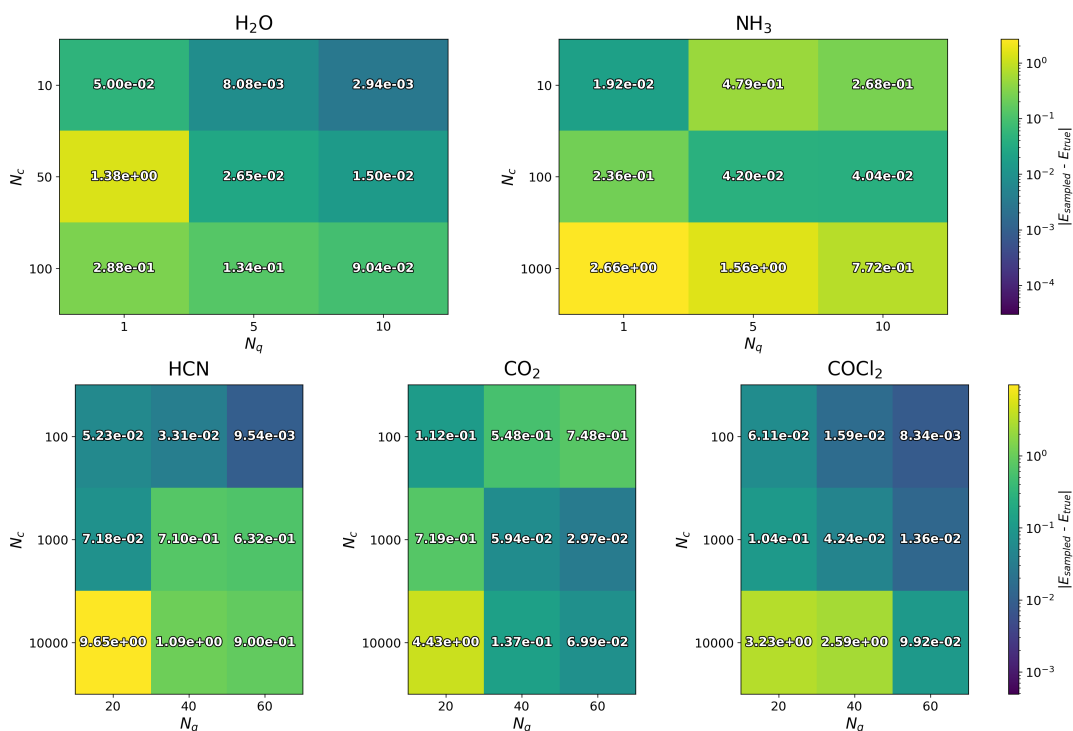
In the infinite-shot limit, enlarging the hybrid basis should not worsen the variational ground-state energy; this behavior is consistent with the discussion in Sec. II. Once sampling noise is introduced, however, the generalized eigenproblem need not remain strictly variational. In that regime, adding additional classical or quantum directions can amplify the effect of noise and increase the final energy error rather than improve the solution. To examine this behavior systematically, we varied the numbers of classical and quantum states, N_c and N_q , and computed the resulting ground-state errors for all benchmark molecules.

For each molecule, we evaluated the ground-state energy error on a grid of truncated classical and quantum subspace sizes (N_c, N_q) at fixed shot counts of 10^3 and 10^7 , as shown in the two figures below. For each case, we formed the sampled generalized eigenvalue problem

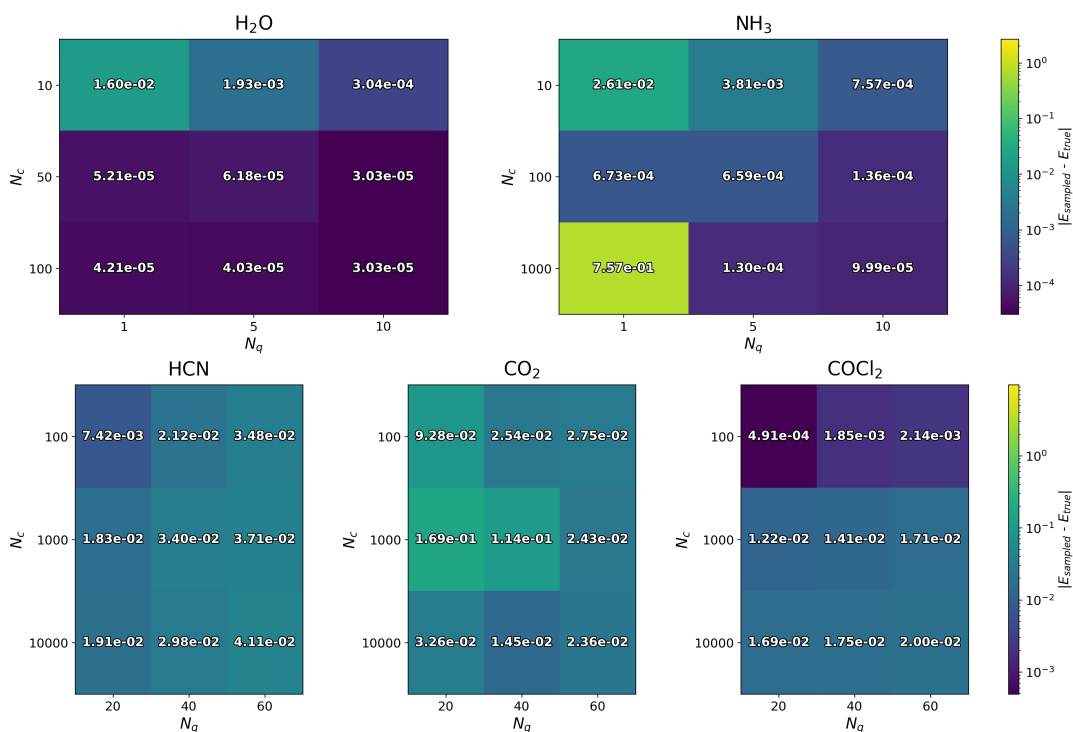
$$Hx = ESx, \quad S = \begin{pmatrix} I & S_{cq} \\ S_{cq}^\dagger & S_{qq} \end{pmatrix}, \quad H = \begin{pmatrix} H_{cc} & H_{cq} \\ H_{cq}^\dagger & H_{qq} \end{pmatrix},$$

where the required blocks were obtained by truncating the stored sampled matrices to the first N_c classical states and first N_q quantum states. The assembled matrices were Hermitized before solution, and the lowest generalized eigenvalue was computed with the LOBPCG solver using $\text{tol} = 10^{-8}$ and $\text{maxiter} = 300$, with multiple random complex initial vectors for robustness. The resulting sampled ground-state energy E_{sampled} was compared against the precomputed reference energy E_{true} (ground state energy from SHCI), and each heatmap entry reports the mean value of $|E_{\text{sampled}} - E_{\text{true}}|$ over independent random-seed realizations. The cell colors use a logarithmic scale, and the printed values are the corresponding mean absolute errors in scientific notation.

The resulting heatmaps show a clear difference between the low- and high-shot regimes. At the lower shot count, $n_{\text{shot}} = 10^3$, increasing N_c or N_q does not systematically improve the ground-state energy error, and larger subspaces often provide little benefit or even worsen the result. In this regime, sampling noise is large enough that the sampled generalized eigenproblem no longer cleanly reflects the variational advantage of additional basis directions. At the higher shot count, $n_{\text{shot}} = 10^7$, the benefit of enlarging the hybrid basis becomes more visible, especially for the smaller systems, where lower error regions extend more clearly toward larger N_c and N_q . The larger systems also improve relative to the 10^3 -shot case, but the trend remains less pronounced, indicating that noise is reduced yet still significant enough to mask the full advantage of additional classical and quantum directions. This indicates that reducing the ground-state energy error depends not only on the number of retained states, but also on the quality of those states as an effective variational basis in the presence of sampling noise.

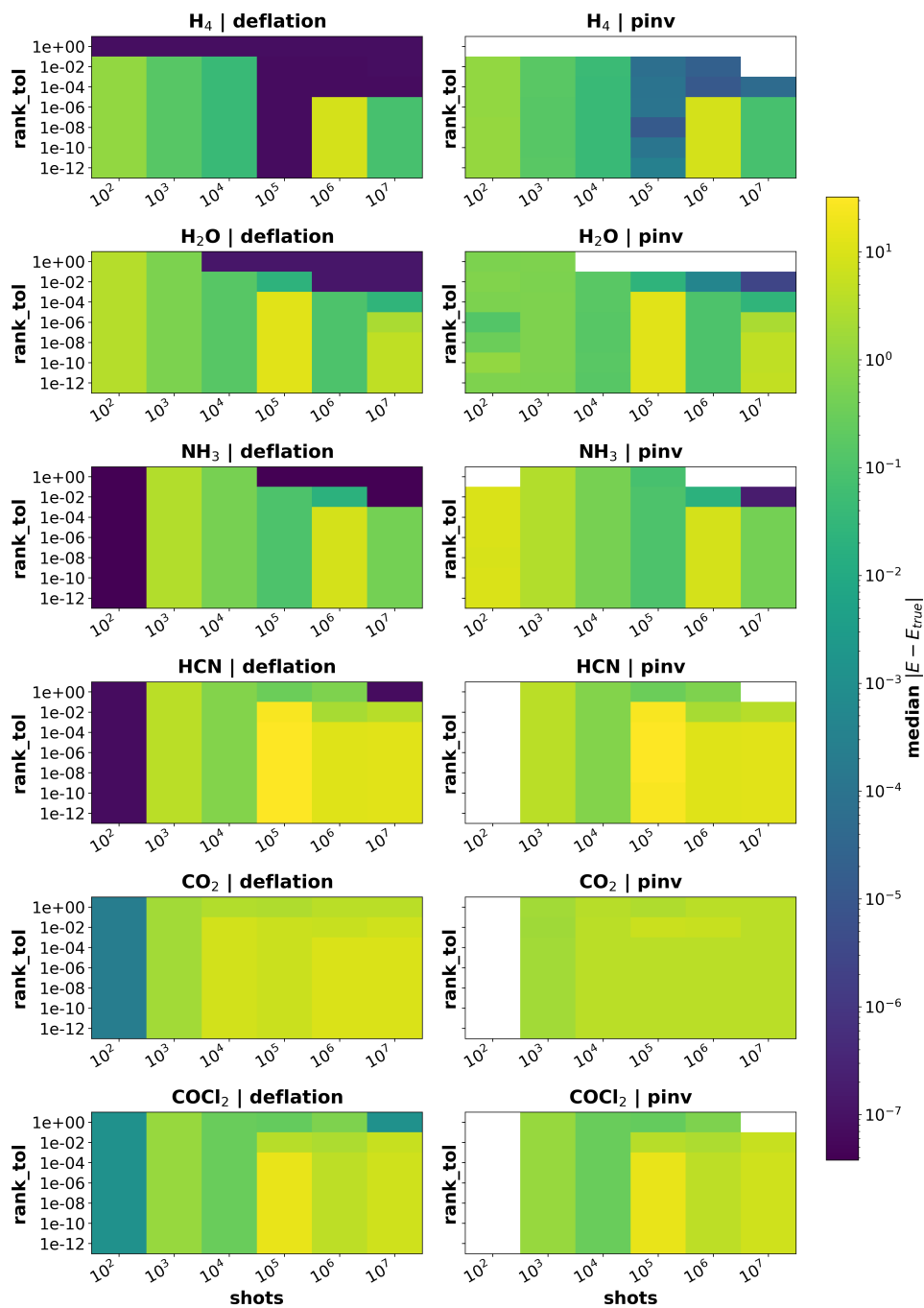


Supplementary Figure S1. Ground-state energy error over the (N_c, N_q) grid at fixed shot count $n_{\text{shot}} = 10^3$.



Supplementary Figure S2. Ground-state energy error over the (N_c, N_q) grid at fixed shot count $n_{\text{shot}} = 10^7$.

Appendix D: Threshold dependence of Schur-complement eigensolvers for sampled matrices



Supplementary Figure S3. Threshold dependence of sampled-matrix Schur-complement eigensolvers. Rows correspond to benchmark molecules, columns to deflation and pseudo-inverse regularization, and color to the median absolute ground-state energy error. White cells indicate parameter settings where the pinv Schur-complement solver returned no finite value because all Schur-complement directions were removed by the threshold.

For each molecule, shot count, and random seed, we formed the sampled overlap matrix and built the corresponding Schur-complement block used by the deflation and pseudo-inverse solvers. We then swept the threshold parameter `rank_tol` over the values shown on the vertical axis and solved the thresholded generalized eigenvalue problem with either deflation or pseudo-inverse regularization. For each threshold, this gives a ground-state energy estimate, which we compare with the SHCI reference energy. The color plotted in Figure S3 is the median absolute energy error over seeds, so each heatmap shows how the solver accuracy changes jointly with shot count and threshold. The horizontal axis is the number of shots, the vertical axis is the chosen threshold, and the two columns compare deflation with pseudo-inverse regularization.

Appendix E: Shot-count extrapolation with qubit number

Figure S4 was constructed from the per-molecule energy-error curves shown in of Figure 3(d). For each molecule, we considered the curve of mean absolute energy error, $|\Delta E|$, versus shot count and formed its lower envelope, so that only the best achieved error up to each shot level was retained. Chemical accuracy was defined as 1.5936×10^{-3} Ha, and the corresponding shot cost, $\text{shots}_{\text{acc}}^{\text{chem}}$, was estimated as the shot count at which the lower-envelope curve reaches this threshold. Here, the shot count is the per-histogram shot count appearing on the horizontal axis of Figure 3(d). The corresponding total cost for the full classical-quantum block is obtained by multiplying this value by $N_q(1 + 2B)$, since each quantum basis state requires one reference histogram and $2B$ interference histograms. When the threshold was crossed within the measured shot range, the crossing point was obtained by log-log interpolation between neighboring data points. When the threshold was not reached, the shot cost was estimated by log-log extrapolation of the lower-envelope trend. This extrapolation assumes that any plateau in the histogram-sampling curve, with shot count on the horizontal axis and energy error on the vertical axis, is eventually improved at higher shot count so that the lower-envelope error continues to decrease.

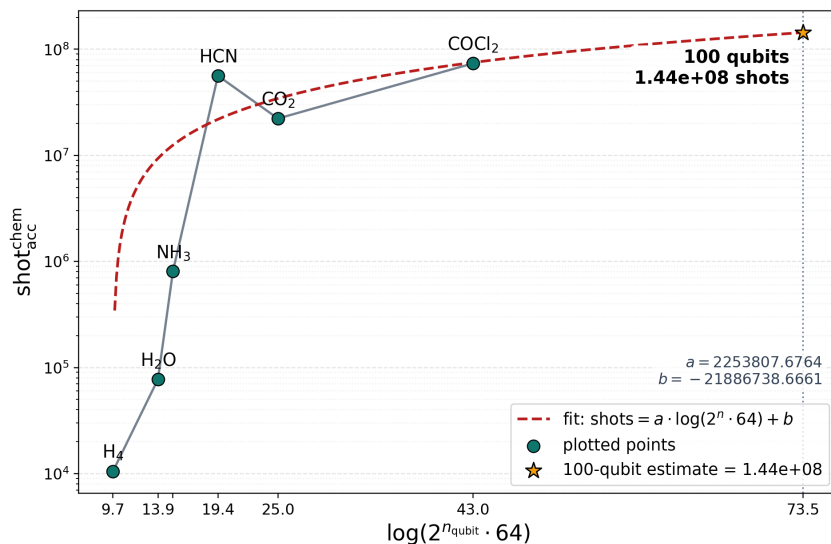
To compare molecules on the same theoretical footing, these shot costs were then normalized to a common $N_q = 64$ using

$$\text{shots}_{\text{adj}} = \text{shots}_{\text{orig}} \frac{\log(2^{n_{\text{qubit}}} \cdot 64)}{\log(2^{n_{\text{qubit}}} \cdot N_q^{\text{current}})}.$$

After this normalization, we plotted the adjusted chemical-accuracy shot cost against the theoretical variable $\log(2^{n_{\text{qubit}}} \cdot 64)$ and fit the data with the model

$$\text{shot}_{\text{acc}}^{\text{chem}} = a \log(2^{n_{\text{qubit}}} \cdot 64) + b.$$

This fit is applied at the per-quantum-state, per-histogram sample-complexity level, before converting to the total classical-quantum-block cost through the factor $N_q(1 + 2B)$. In this corrected model, the 100-qubit extrapolation is approximately 1.44×10^8 shots per histogram. Multiplying by $N_q(1 + 2B)$ then gives a total classical-quantum block cost of order 10^{10} shots. This estimate is based on the present workflow and does not include possible further reductions from more advanced factorization or compression strategies.



Supplementary Figure S4. Normalized chemical-accuracy shot cost versus $\log(2^{n_{\text{qubit}}} \cdot 64)$. Points are the adjusted per-histogram shot costs, the solid line is the fitted model, and the star marks the extrapolated 100-qubit estimate.

Appendix F: Error-rate requirements for CANOE state preparation

CANOE can be implemented at either the physical-qubit or logical-qubit level, so the error rate p may denote either the physical error rate p_{phys} or the logical error rate p_{logic} . Let δ denote the allowed failure probability for a single sampling run. Under a worst-case assumption, the required error rate is bounded by

$$\delta \geq 1 - (1 - p)^{D_{\text{gate}}},$$

where D_{gate} is the circuit gate depth. Assuming that the coherence time is much longer than the gate time, decoherence can be neglected and p can be interpreted as a gate error rate.

The quantum states prepared in CANOE are Krylov states

$$|q_k\rangle = (e^{-iH\Delta t})^k |q_0\rangle,$$

which can be first-order Trotterized as

$$|q_k\rangle \approx \left(\prod_{\ell=1}^L e^{-iH_\ell \delta t} \right)^{kr} |q_0\rangle,$$

where $H_\ell = h_\ell P_\ell$. In a naive second-quantized formulation, $L \sim n_{\text{qubit}}^4$, so

$$D_{\text{gate}} \approx Lrk.$$

For a FeMoco-scale estimate [49, 53–55], taking $k = 64$, $n_{\text{qubit}} \sim 100$, and $r \sim 10$ gives $D_{\text{gate}} \sim 10^{11}$. With $\delta \sim 10^{-3}$, this yields the conservative bound

$$p \lesssim 10^{-14}.$$

This estimate is highly conservative. Using optimized Hamiltonian factorizations, such as integral tensor factorization [46], can reduce L to $O(n_{\text{qubit}})$, leading instead to a weaker bound

$$p \lesssim 10^{-8}.$$

-
- [1] Y. Alexeev, V. S. Batista, N. Bauman, L. Bertels, D. Claudino, R. Dutta, L. Gagliardi, S. Godwin, N. Govind, M. Head-Gordon, *et al.*, *Journal of Chemical Theory and Computation* **21**, 11335 (2025).
- [2] Y. Alexeev, M. Amsler, M. A. Barroca, S. Bassini, T. Battelle, D. Camps, D. Casanova, Y. J. Choi, F. T. Chong, C. Chung, *et al.*, *Future Generation Computer Systems* **160**, 666 (2024).
- [3] K. Gratsea and M. Otten, arXiv preprint arXiv:2510.26547 (2025).
- [4] B. P. Lanyon, J. D. Whitfield, G. G. Gillett, M. E. Goggin, M. P. Almeida, I. Kassal, J. D. Biamonte, M. Mohseni, B. J. Powell, M. Barbieri, A. Aspuru-Guzik, and A. G. White, *Nature Chemistry* **2**, 106 (2010).
- [5] A. Peruzzo, J. McClean, P. Shadbolt, M.-H. Yung, X.-Q. Zhou, P. J. Love, A. Aspuru-Guzik, and J. L. O’Brien, *Nature Communications* **5**, 4213 (2014).
- [6] J. Tilly, A. Z. Foreman, J. Helsen, C. Huang, D. W. Berry, N. Wiebe, J. R. McClean, and T. E. O’Brien, *Physics Reports* **986**, 1 (2022).
- [7] M. Mohseni, A. Scherer, K. G. Johnson, O. Wertheim, M. Otten, N. A. Aadit, Y. Alexeev, K. M. Bresniker, K. Y. Camsari, B. Chapman, S. Chatterjee, G. A. Dagnew, A. Esposito, F. Fahim, M. Fiorentino, A. Gajjar, A. Khalid, X. Kong, B. Kulchytskyy, E. Kyoseva, R. Li, P. A. Lott, I. L. Markov, R. F. McDermott, G. Pedretti, P. Rao, E. Rieffel, A. Silva, J. Sorebo, P. Spentzouris, Z. Steiner, B. Torosov, D. Venturelli, R. J. Visser, Z. Webb, X. Zhan, Y. Cohen, P. Ronagh, A. Ho, R. G. Beausoleil, and J. M. Martinis, arXiv preprint: 2411.10406 (2024), 2411.10406 [quant-ph].
- [8] J. R. McClean, M. E. Kimchi-Schwartz, J. Carter, and W. A. de Jong, *Physical Review A* **95**, 042308 (2017).
- [9] Y. Hao, Q. Ding, X. Wang, and X. Yuan, *Journal of Chemical Theory and Computation* **22**, 859 (2026).
- [10] H. R. Grimsley, S. E. Economou, E. Barnes, and N. J. Mayhall, *Nature Communications* **10**, 3007 (2019).
- [11] W. J. Huggins, J. R. McClean, N. C. Rubin, Z. Jiang, N. Wiebe, K. B. Whaley, and R. Babbush, *New Journal of Physics* **22**, 073009 (2020).
- [12] M. Otten, S. K. Gray, D. A. Fedorov, and Y. Alexeev, *Journal of Chemical Theory and Computation* **18**, 7205 (2022).
- [13] D. A. Fedorov, Y. Alexeev, S. K. Gray, and M. Otten, *Quantum* **6**, 703 (2022).
- [14] H. Zhang and A. Asthana, arXiv:2509.13096 (2025).

- [15] R. Shaydulin, C. Li, S. Chakrabarti, M. DeCross, D. Herman, N. Kumar, J. Larson, D. Lykov, P. Minssen, Y. Sun, *et al.*, *Science Advances* **10**, eadm6761 (2024).
- [16] U. Baek, J. Lee, W. J. Huggins, and K. B. Whaley, *PRX Quantum* **4**, 030307 (2023).
- [17] R. M. Parrish and P. L. McMahon, arXiv preprint arXiv:1909.08925 (2019).
- [18] N. H. Stair, R. Huang, and F. A. Evangelista, arXiv preprint arXiv:1911.05163 (2019).
- [19] K. Klymko, C. Mejuto-Zaera, S. J. Cotton, F. Wudarski, M. Urbanek, D. Hait, M. Head-Gordon, K. B. Whaley, J. Moussa, N. Wiebe, W. A. de Jong, and N. M. Tubman, *PRX Quantum* **3**, 020323 (2022).
- [20] N. Yoshioka, M. Amico, W. Kirby, P. Jurcevic, A. Dutt, B. Fuller, S. Garion, H. Haas, I. Hamamura, A. Ivrii, R. Majumdar, Z. Mineev, M. Motta, B. Pokharel, P. Rivero, K. Sharma, C. J. Wood, A. Javadi-Abhari, and A. Mezzacapo, *Nature Communications* **16**, 5014 (2025).
- [21] C. L. Cortes and S. K. Gray, *Physical Review A* **105**, 022417 (2022).
- [22] S. Patel, P. Jayakumar, R. Huang, T. Zeng, and A. F. Izmaylov, arXiv preprint arXiv:2509.01061 (2025).
- [23] J. Robledo-Moreno, M. Motta, H. Haas, A. Javadi-Abhari, P. Jurcevic, W. Kirby, S. Martiel, K. Sharma, S. Sharma, T. Shirakawa, I. Sitdikov, R.-Y. Sun, K. J. Sung, M. Takita, M. C. Tran, S. Yunoki, and A. Mezzacapo, *Science Advances* **11**, eadu9991 (2025).
- [24] E. N. Epperly, L. Lin, and Y. Nakatsukasa, *SIAM Journal on Matrix Analysis and Applications* **43**, 1263 (2022).
- [25] K. Kanno, M. Kohda, R. Imai, S. Koh, K. Mitarai, W. Mizukami, and Y. O. Nakagawa, arXiv preprint arXiv:2302.11320 (2023).
- [26] J. Haah, A. W. Harrow, Z. Ji, X. Wu, and N. Yu, *IEEE Transactions on Information Theory* **63**, 5628 (2017).
- [27] H.-Y. Huang, R. Kueng, and J. Preskill, *Nature Physics* **16**, 1050 (2020).
- [28] H.-Y. Huang, R. Kueng, and J. Preskill, arXiv:2103.07510 (2021).
- [29] A. Gresch and M. Kliesch, *Nature Communications* **16**, 689 (2025).
- [30] H. Ren, Y. Zhang, W. M. Billings, R. Tomann, N. V. Tkachenko, M. Head-Gordon, and K. B. Whaley, arXiv preprint arXiv:2504.16008 (2025), version 2.
- [31] G. H. Golub and C. F. V. Loan, *Matrix Computations*, 4th ed. (Johns Hopkins University Press, Baltimore, MD, 2013).
- [32] Y. Saad, *Numerical Methods for Large Eigenvalue Problems*, 2nd ed. (Society for Industrial and Applied Mathematics, Philadelphia, PA, 2011).
- [33] A. V. Knyazev, *SIAM Journal on Scientific Computing* **23**, 517 (2001).
- [34] G. S. Ravi, P. Gokhale, Y. Ding, W. Kirby, K. Smith, J. M. Baker, P. J. Love, H. Hoffmann, K. R. Brown, and F. T. Chong, in *Proceedings of the 28th ACM International Conference on Architectural Support for Programming Languages and Operating Systems, Volume 1* (2022) pp. 15–29.
- [35] R. Orús, *Annals of physics* **349**, 117 (2014).
- [36] A. Kandala, A. Mezzacapo, K. Temme, M. Takita, M. Brink, J. M. Chow, and J. M. Gambetta, *Nature* **549**, 242 (2017).
- [37] Y. Shen, K. Klymko, J. Sud, D. B. Williams-Young, W. A. de Jong, and N. M. Tubman, *Quantum* **7**, 1066 (2023).
- [38] J. Li, M. Otten, A. A. Holmes, S. Sharma, and C. J. Umrigar, *The Journal of chemical physics* **149** (2018).
- [39] J. W. Mullinax and N. M. Tubman, *The Journal of Chemical Physics* **162** (2025).
- [40] D. Patel, L. Clinton, S. T. Flammia, and R. García-Patrón, arXiv:2602.09119 (2026).
- [41] J. Lee, W. J. Huggins, M. Head-Gordon, and K. B. Whaley, *Journal of Chemical Theory and Computation* **15**, 311 (2019).
- [42] M. O. Zhang Hao, arXiv:2511.14734 (2025).
- [43] C. Hicks and D. Lee, *Physical Review Research* **5**, L022001 (2023).
- [44] Q. Li, A. Vidwans, Y. Wang, and M. B. Soley, arXiv preprint arXiv:2507.23074 (2025), arXiv:2507.23074 [quant-ph].
- [45] D. Wecker, M. B. Hastings, and M. Troyer, *Physical Review A* **92**, 042303 (2015).
- [46] W. J. Huggins, J. R. McClean, N. C. Rubin, Z. Jiang, N. Wiebe, K. B. Whaley, and R. Babbush, *npj Quantum Information* **7**, 23 (2021).
- [47] L. Lin, arXiv preprint arXiv:2201.08309 (2022).
- [48] B. F. Schiffer, D. S. Wild, N. Maskara, M. D. Lukin, and J. I. Cirac, arXiv preprint arXiv:2506.18765 (2025).
- [49] M. Reiher, N. Wiebe, K. M. Svore, D. Wecker, and M. Troyer, *Proceedings of the National Academy of Sciences* **114**, 7555 (2017).
- [50] G. H. Low, R. King, D. W. Berry, Q. Han, A. E. De-Prince III, A. F. White, R. Babbush, R. D. Somma, and N. C. Rubin, *Physical Review X* **15**, 041016 (2025).
- [51] F. Alam, J. L. Bosse, I. Čepaitė, A. Chapman, L. Clinton, M. Crichigno, E. Crosson, T. Cubitt, C. Derby, O. Dowinton, P. K. Faehrmann, S. Flammia, B. Flynn, F. M. Gambetta, R. García-Patrón, M. Hunter-Gordon, G. Jones, A. Khedkar, J. Klassen, M. Kreshchuk, E. H. McMullan, L. Mineh, A. Montanaro, C. Mora, J. J. L. Morton, D. Patel, P. Rolph, R. A. Santos, J. R. Seddon, E. Sheridan, W. Somogyi, M. Svensson, N. Vaishnav, S. Y. Wang, and G. Wright, arXiv:2510.26845 (2025).
- [52] A. Elben and B. Vermersch, arXiv preprint arXiv:2509.12749 (2025).
- [53] J. M. Montgomery and D. A. Mazziotti, *The Journal of Physical Chemistry A* **122**, 4988 (2018).
- [54] Z. Li, J. Li, N. S. Dattani, C. J. Umrigar, and G. K.-L. Chan, *The Journal of Chemical Physics* **150**, 024302 (2019).
- [55] J. Lee, D. W. Berry, C. Gidney, W. J. Huggins, J. R. McClean, N. Mosonyi, N. C. Rubin, N. Wiebe, and R. Babbush, *PRX Quantum* **2**, 030305 (2021).